Journal of Materials Research and Technology 38 (2025) 2534–2555

Contents lists available at ScienceDirect

Journal of Materials Research and Technology

journal homepage: www.elsevier.com/locate/jmrt

Hydroxyapatite-doped coatings with antimicrobial properties by matrix assisted pulsed laser evaporation

Diana-Elena Radulescu [a], Bogdan Stefan Vasile [b,c,d,*], Vasile-Adrian Surdu [a,e], Roxana Doina Trusca [b], Alexandra Catalina Birca [b,c], Cornelia-Ioana Ilie [a,c], Lia-Mara Ditu [f], Ludmila Motelica [b], Ionela Andreea Neacsu [a,c], Iulian Boerasu [b], Simona Brajnicov [g], Cosmin Iulian Codrea [h], Ecaterina Andronescu [a,c,d]

[a] Department of Science and Engineering of Oxide Materials and Nanomaterials, Faculty of Chemical Engineering and Biotechnologies, National University of Science and Technology POLITEHNICA Bucharest, 011061, Bucharest, Romania
[b] Research Center for Advanced Materials, Products and Processes, National University of Science and Technology POLITEHNICA Bucharest, 060042, Bucharest, Romania
[c] National Research Center for Micro and Nanomaterials, Faculty of Chemical Engineering and Biotechnologies, National University of Science and Technology POLITEHNICA Bucharest, 060042, Bucharest, Romania
[d] Academy of Romanian Scientists, 050045, Bucharest, Romania
[e] Department of Materials Science, Faculty of Materials Science and Engineering, Transilvania University of Brasov, 29 Eroilor Blvd., 500036, Brasov, Romania
[f] Department of Botany and Microbiology, Faculty of Biology, University of Bucharest, 060101, Bucharest, Romania
[g] Natl Inst Lasers Plasma & Radiat Phys, Lasers Dept, Magurele, 077125, Romania sau, 409 Atomistilor Str, Magurele, 077125, Romania
[h] Institute of Physical Chemistry, Romanian Academy, Spl. Independentei 202, 060021, Bucharest, Romania

ARTICLE INFO

Keywords:
Hydroxyapatite
Ion substitution
Bioactivity
Coatings
MAPLE
Eggshells
Mussel shells
Biofilm

ABSTRACT

The development of bioactive coatings that improve implant performance is critical due to bacterial colonization, biofilm formation, foreign body responses, and inadequate tissue integration for biomedical applications. To address these issues, this study aimed to synthesize and characterize hydroxyapatite (HAp) coatings derived from biogenic sources (eggshells and mussel shells). Both unsubstituted and Mg^{2+}, Sr^{2+}, and Cu^{2+}-substituted HAp materials were synthesized and deposited on three different substrates: two magnesium-based alloys and titanium. Structural and chemical analyses using X-Ray Diffraction (XRD) and Fourier-Transform Infrared Spectroscopy (FTIR) confirmed successful HAp formation, while Scanning Electron Microscopy (SEM) revealed morphological variations influenced by the biogenic source and dopant concentration. XRD analysis showed that Cu^{2+} doping reduced crystallinity by 15–20 % compared to undoped HAp, while Mg^{2+} and Sr^{2+} maintained structural integrity within 5 % of undoped samplesAccording to biological evaluations, Mg substrates (I and II) reduced *S. aureus* biofilms by up to 8 CFU/mL, while the titanium substrate (III) demonstrated 25–30 % higher cell viability compared to Mg substrates. Further, substrate II increased its biocompatibility by 33 % from 24h to 48h (120 %–160 %). Mg^{2+} and Sr^{2+} substitutions enhanced cell proliferation, while Cu^{2+} presented a dose-dependent cytotoxicity. These findings suggest that biogenic HAp coatings, with personalized composition and substrates, have good potential as multifunctional materials for inhibiting bacterial colonization and promoting osseointegration, offering valuable insights for tissue engineering and regenerative medicine.

1. Introduction

Regenerative medicine, particularly bone tissue engineering, has generated a lot of attention, with the goal of regenerating tissue or treating injured bones. This domain concentrated on the utilization of calcium-based materials, notably hydroxyapatite (HAp). This ceramic material is preferred due to its similarity with the natural apatite from the osseous tissues. Further, HAp is well known for its biocompatibility,

* Corresponding author. Research Center for Advanced Materials, Products and Processes, National University of Science and Technology POLITEHNICA Bucharest, 060042, Bucharest, Romania.
E-mail addresses: radulescu.diana95@gmail.com (D.-E. Radulescu), bogdan.vasile@upb.ro (B.S. Vasile), cornelia_ioana.ilie@upb.ro (C.-I. Ilie), lia-mara.ditu@bio.unibuc.ro (L.-M. Ditu), codrea.cosmin@yahoo.com (C.I. Codrea).

https://doi.org/10.1016/j.jmrt.2025.08.093
Received 25 April 2025; Received in revised form 6 August 2025; Accepted 13 August 2025
Available online 14 August 2025

superior biocompatibility and osteogenic properties. Its applicability as coating materials on the surface of the implant has increased the interest of researchers to develop novel applications to enhance biological performance and improve the functionality of the biomedical devices [1]. Another important property of HAp is the superior bioactivity offering the capacity of creating bonds with the surrounding environment. Nevertheless, the chemical synthesis of HAp is limited due to the high costs and the brittle nature [2–4]. However, the main advantage of this material is its capacity to promote calcium and phosphate ions into the body, thus enhancing the biomineralization process on the surface of the implant [5].

Lately, researchers have focused on the development of HAp using biogenic sources, such as bio-wastes (animal bone, fish bone, eggshells, seashells) to increase the biocompatibility and ability to mimic the chemical structure of human bone leading to an increased tissue regeneration [6–10]. Karunakaran et al. [11] also confirmed the superior bioactivity in comparison with the chemically synthesized HAp, and natural-based HAp. This enhanced bioactivity is due to the presence of several trace elements, such as sodium (Na), magnesium (Mg) and strontium (Sr), generally encountered in the human body [12]. For example, the human bone mineral is a nonstoichiometric apatite is also constituted from trace elements of Zn, Na, Fe, Mg, Sr, etc., while chemically synthesized HAp has no trace elements and may possess low crystal defects. This difference may also be an important factor in the mechanical properties of the developed ceramic material and its applicability. Synthetic HAp has several disadvantages, such as poor mechanical strength and reduced bacterial resistance, limiting load-bearing applications. To surpass these limitations, in the HAp structure can be incorporated metallic or non-metallic ions such as Zn^{2+}, Fe^{3+}, Mg^{2+}, Ag^{2+}, Sr^{2+}, Cu^{2+}, etc as HAp possesses a ion exchange capacity and crystal structure composed of OH^{-}, Ca^{2+}, and $(PO_4)^{3-}$ [13]. To support this, Uysal et al. [14] stated that the ion substitution improved biological, mechanical and antibacterial properties of substituted HAp. Further, they may enhance the osteoinductive and osteoconductive properties of the obtained material. The optimum dopant should enhance the abovementioned properties without negatively influencing the biological performance of the substituted material. Moreover, a suitable concentration of doping ion could provide improved mechanical properties [15].

In this direction, Mg-substituted HAp has proved to be an effective solution to improve bone regeneration. Mg is well known for its applicability in osteoporosis treatments. Further, low concentrations of Mg showed their capacity to stimulate osteoblast proliferation. On the other hand, a high concentration of Mg may reduce the crystallinity of HAp and at the same time increase $(HPO_4)^{2-}$, thus increasing the dissolution [15–17]. Another preferred substituting ion is strontium (Sr), known for its capacity to enhance osteoblasts proliferation and differentiation [18, 19]. This trace element presents the ability to lower the risk of bone fractures and the development of osteoporosis. Additionally, Sr has great influence in the prevention of bone loss by decreasing the activity and differentiation of osteoclasts, while also reducing the production of matrix metalloproteinase in osteoblasts. Moreover, by adding this doping ion to the HAp structure, the microstructure, morphology, solubility, thermal stability, and mechanical properties are influenced. This makes it an effective approach to achieve specific characteristics in the biomaterial tailored to its intended use [20–22]. Furthermore, Cu^{2+} ions substitution into the HAp structure demonstrated positive effects on cell growth, angiogenesis, cell migration, and stem cell differentiation, while also inhibiting osteoclast activity. To explore these biological effects further, Ressler et al. [23] created Cu-doped HA through the precipitation method, where Cu^{2+} substituted calcium ions. They also experimented obtaining the substituted material through the immersion method of non-doped HA in a Cu^{2+} ion solution, leading to substitutions at the hydroxyl (OH) sites. Although high concentrations of Cu^{2+} showed strong antibacterial properties, they also reported toxicity risks. Therefore, it's important to choose appropriate concentration to promote cell growth effectively [23,24].

Osteoconductive biomaterials are often used as coatings for metal implants to improve their clinical durability. HAp is a commonly used material for this purpose, either applied as a thin film or coating on metal surfaces for the improvement of bioactivity and to ensure long-lasting osteoconductivity. Due to its similarity in chemical structure, crystallographic composition, and mineral content with the native apatite, this biomaterial creates a chemical bond between the implant surface and natural bone. These bonds aid the stimulation of bone growth and enhance the integration of human bone tissues with the implant [25]. For example, Akazawa [26] mentioned that the attachment of a coating onto the surface of the implant leads to the improvement of bone regeneration process in the damaged sites. Furthermore, these types of coatings present the capacity to improve the biological functions of medical devices. Considering the functionality in the medical field, Liao et al. [27] mentioned that HAp coatings are necessary to reduce the degradation rate of the implanted medical device into the human body. HAp films present the capacity to create suitable bonds between the surrounding tissue and metal substrate. Additionally, HAp-coated metallic surfaces attracted great attention and are steadily being researched due to metallic implant strength and improved bioactivity generated by the ceramic material, thus enhancing the implant adhesion and functional link structure [27,28].

The proper material selection and efficient coating development are critical to decreasing implant failure risks. Furthermore, improved surface roughness promotes superior coating adherence and is essential for a variety of applications, as it greatly expands the surface area using etching or deposition processes [29]. While these surface modifications improve the mechanical properties and coating adhesion, the biocompatibility of the materials must be also considered. Hosseini et al. [30] suggested that wear-induced ion release must be carefully evaluated in orthopaedic applications such as joint replacement, since high concentrations of these ions can cause toxic reactions, allergic responses, and pathological conditions. As a result, surface modification of alloys will be needed in order to overcome these restrictions, and to improve overall implant performance and functioning.

Regarding the surface of the coating, metallic biomaterials such as titanium (Ti) and its alloys demonstrated excellent physical properties. Over the years, they exhibited great biocompatibility, outstanding corrosion resistance, and low modulus of elasticity in contact with body fluids, highlighting their functionality as preferred materials for human implantation [31]. Nonetheless, Ti alloys also presented poor osseointegration. Therefore, applying a protective biocompatible coating was proved to be the ideal method to minimize corrosion and improve the surface properties. In this direction, HAp application on the surface of the implant led to enhanced biological activity. This application can be done through various methods, such as the vapor deposition, sol-gel method, electrophoretic and plasma deposition on the implant surfaces [32–34].

Further, Mg-based alloys have shown remarkable results due to their controlled degradation rate, superior mechanical properties and non-toxicity. Li et al. [16] confirmed that these alloys encourage osteogenesis by enabling direct bone contact with the implant. Nevertheless, their quick corrosion in physiological environments may lead to localized increases in pH and faster hydrogen production, which may negatively affect the long-term mechanical performance of the implant [16, 17]. A rigorous control of the coating and good adherence may be obtained by applying the latest technological advances.

Researchers concentrated on many different types of surface technologies, such as plasma spraying, electrochemical deposition, magnetron sputtering, physical vapor deposition, or chemical vapor deposition, and pulsed laser deposition (PLD). Safavi mentioned that electrodeposition has established great importance for surface modifications techniques of synthetic biomaterials. The process allows fabrication of homogeneous layers and adding one or more reinforcing agents into the expanding film [35]. On the other hand, Su et al. [36]

mentioned that plasma-sprayed HAp coatings have the potential to improve the substrate's bonding strength and extend their lifespan after implantation. As is well known, this approach is frequently used in the orthopaedics area because it increases the bonding strength of coating even though the high spraying temperature of the HAp coatings also resulted in an imperfect coating structure. Pulsed-laser ablation has been applied as a vacuum-based coating technique for surface modification. Droplets from the target materials are deposited, which is one of the PLD coating method's most significant disadvantages. In a typical pulsed-laser ablation, atoms, ions, and micrometre-sized molten droplets are all concurrently blasted from targets [37]. Although laser ablation enables accurate material removal, its use may be restricted by the equipment's complexity and expense as well as the possibility of substrate damage. Sun [38] reported that this method lead to generation of porous surfaces with defects induced by the thermal effect. In contrast, By operating at lower temperatures, minimizing thermal stress on substrates, and providing exact control over the deposition process, RF magnetron sputtering creates stable and effective coatings. This method is appropriate for biomedical applications since it makes it possible to create dense, homogeneous, and adhered coatings with controlled thickness and composition [39,40]. In this case, the matrix-assisted pulsed laser evaporation (MAPLE) deposition method has been the most suitable and effective. This technique is solvent-free, specifically used to achieve ultra-thin, well adherent and homogeneous coatings on numerous types of substrates, without altering the chemical and physical properties of the deposited material. Furthermore, MAPLE provides outstanding film adhesion to the substrate and a controlled deposited layer thickness (varying from a few tens of nanometers to 1 μm) [41,42]. Consequently, this method ensures an ideal design of surface characteristics in terms of coating adhesion on the surface of an implant, and a suitable control on the antibacterial properties.

Although previous studies focused on the development of chemically synthesized HAp coatings on numerous substrates, few researchers presented the synergistic effect between the source of CaO precursors, substituting ion, and the type of substrate. This work has significant interest because it uses bio-waste sources as CaO precursors to synthesize ion-doped HAp coatings using MAPLE. In comparison to chemically manufactured HAp, this biogenic technique maintains the natural trace elements, which improve biocompatibility and simulate bone regeneration. The integration of biogenic sources, ion doping, and comprehensive assessment of diverse substrates, such as Mg-based alloys and Ti, defines a novel approach for environmentally friendly implant surface modificationThe aim of this study is to develop thin films based on doped-HAp material on different substrates for biofilm modulation. In this regard, undoped and Cu, Sr, and Mg-doped HAp have been synthesized for the application on the substrates. Further, three substrates (I – MgZnMn (Mn 0.62 Zn 4.3), II - MgZnMnY (Zn 7.1 Mn 1.17 Y 1.2) and III – Ti) were selected to identify the ideal surface to be further considered for bone tissue engineering. All the obtained coatings were investigated considering their morpho-structural properties and biological activity, respectively the antibacterial and cellular viability.

2. Materials and methods

2.1. Materials

Mussel shells and eggshells were procured from a local restaurant to be used as calcium oxide sources. For the synthesis of doped HAp, the following precursors were used: $(NH_4)_2HPO_4$ (98 %), NH_4OH, $Sr(NO_3)_2$ (98 %), $Cu(NO_3)_2$ •$2.5H_2O$, $(NH_4)_2HPO_4$ (98 %), $MgCl_2$•$6H_2O$ (99 %) from Sigma–Aldrich, Saint Luis, MO, USA, and distilled water. Further, fetal bovine serum, DMEM medium (Sigma-Aldrich, Saint Luis, MO, USA), and XTT reagent (2,3-Bis-(2-Methoxy-4-Nitro-5-Sulfophenyl)-2H-Tetrazolium-5-Carboxanilide) (Thermo Fischer Scientific, Waltham, MA, USA) were used for the XTT Cell Viability Assay. The antibacterial activity was conducted using Nutrient Broth No. 2 and agar from Sigma-Aldrich (Darmstadt, Germany). The strain used in this study is provided by the Microorganisms Collection of the Department of Microbiology, Faculty of Biology, and the Research Institute at the University of Bucharest.

2.2. CaO synthesis

The collected mussel shells were first cleaned with boiled water to eliminate any impurities. Further, they were washed with distilled water and placed in an ultrasonic bath to remove any remaining residues. After washing, the shells were dried in an oven at 60 °C for 48 h and ground into a fine powder. This powder was subsequently heat-treated at 1000 °C for 3 h. For the eggshells, the membrane was initially removed by soaking them in a 0.5 M HCl solution. Once the organic material was eliminated, the same procedure used for the mussel shells was followed.

2.3. Unsubstituted HA and ion-substituted hydroxyapatite synthesis Method from biogenic sources

HAp synthesis was carried out using the co-precipitation method, followed by a microwave-assisted hydrothermal maturation process utilizing the synthWAVE equipment from Milestone Srl in Sorisole, Bergamo, Italy. This approach was chosen for its ability to precisely control nucleation and crystal growth under specific conditions, including regulated pressure and elevated temperature. Researchers have found that the use of microwaves significantly accelerates the synthesis process and enhances its effectiveness. Additionally, the resulting materials exhibit excellent dispersibility and crystallinity [43]. For the co-precipitation, a solution of $(NH_4)_2HPO_4$ was prepared by dissolving 11.04 g in 200 mL of distilled water, as shown in Scheme 1. Simultaneously, 7.8 g of CaO was dispersed in another 200 mL of distilled water. Both types of CaO, sourced from eggshells and mussel shells, were utilized in the experiments. The phosphate solution was added dropwise to the Ca^{2+} dispersion while stirring magnetically at room temperature. During this precipitation phase, the pH was maintained around 9–10. Once the desired pH was achieved, the mixture was transferred to the microwave-assisted hydrothermal equipment for maturation. The synthesis method was conducted under specific conditions, starting with an initial pressure of 2 bars; in 2 min the temperature increased to 120 °C and remained constant for the following 10 min. After the maturation process, the resulting precipitates were filtered and washed with distilled water until neutral pH was reached and then dried in the oven at 60 °C for 48 h.

To obtain the Sr, Cu or Mg-substituted HAp, the process was similar to unsubstituted HAp synthesis. The only difference is presented by the addition of the substituents precursors: $Sr(NO_3)_2$, $MgCl_2$•$6H_2O$ or $Cu(NO_3)_2$. To obtain Sr-substituted, Mg-substituted HAp and Cu-substituted HAp, various quantities of precursors were used corresponding to different Ca^{2+} substitution molar ratio (1 % and 5 %). The substituting ions concentration has been optimized and selected according to previous studies in terms of biologic effect [44–47]. Separate solutions of corresponding precursors were added into the CaO dispersion, under magnetics stirring prior to the addition of phosphate solution. The obtained solutions followed the same process of hydrothermal maturation in the microwave field. Based on the source of the natural source and doping ion, the samples were named as mentioned in Table 1.

2.4. Deposition of obtained samples

2.4.1. Material selection and pre-treatment

Three metallic substrates were selected to evaluate HAp coating performance destined for biomaterial applications and degradation environments well known in orthopaedic and dental implants. The substrate selection approach was created to address the extensive need of modern implant applications, from long-term load-bearing implants to short-term biodegradable devices.

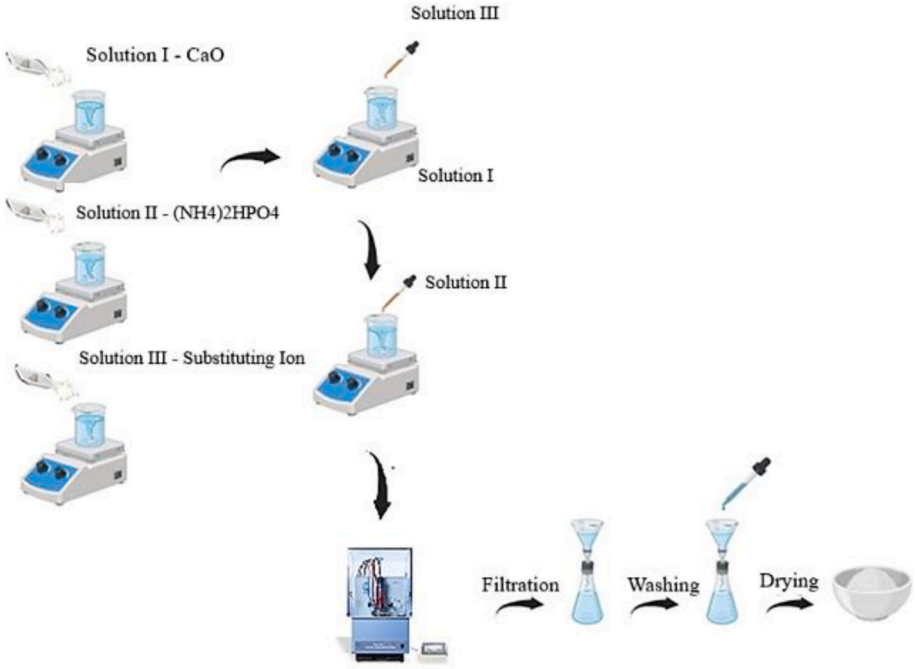

Scheme 1. Schematic representation of unsubstituted and substituted HAp samples.

Table 1
Codification of the synthesized samples (1 % and 5 % represent the concentrations of the substituting ions).

Source	Code	Cu^{2+} (%)	Sr^{2+} (%)	Mg^{2+} (%)
Eggshells (C)	HAp_C	0	0	0
	HAp_Cu_1_C	1	0	0
	HAp_Cu_5_C	5	0	0
	HAp_Sr_1_C	0	1	0
	HAp_Sr_5_C	0	5	0
	HAp_Mg_1_C	0	0	1
	HAp_Mg_5_C	0	0	5
Mussel shells (S)	HAp_S	0	0	0
	HAp_Cu_1_S	1	0	0
	HAp_Cu_5_S	5	0	0
	HAp_Sr_1_S	0	1	0
	HAp_Sr_5_S	0	5	0
	HAp_Mg_1_S	0	0	1
	HAp_Mg_5_S	0	0	5

Substrate I, MgZnMn alloy (Mn 0.62 Zn 4.3), has been selected as a representative of biodegradable implant material. Given its controlled degradation, this material offers the potential of avoiding secondary surgery. Studies demonstrated that the incorporation of manganese leads to an improve in ductility and biocompatibility, while adding zinc improves mechanical properties and has antibacterial benefits [48,49]. In order to preserve coating stability and bioactivity the implant's operational durability, this substrate provides the possibility to assess the therapeutic potential of HAp coatings on a metallic surface with control degradation rates [50]. The development of biodegradable implants presents a fundamental challenge, especially for potential of HAp coatings to modify substrate in controlled degradation rates while maintaining surface bioactivity.

Substrate II, a yttrium-modified MgZnMnY alloy (Zn 7.1 Mn 1.17 Y 1.2), was used to examine the impact of rare earth element additions on coating-substrate interaction and biological performance. In this regards, the incorporation of yttrium into Mg alloys has shown to improve corrosion resistance and significantly enhance mechanical characteristics. This substrate allows the assessment of yttrium presence and its impact on the biocompatibility of the HAp coatings [51–53]. The systematic comparison of substrates I and II offers important information on the optimization of the composition of biodegradable alloys for implant applications that include HAp coatings.

Substrate III (pure titanium) was chosen as the reference standard to act as the established starting point for long-term orthopedic implants. Ti is nowadays the preferred material for evaluating innovative biomaterial systems due to its remarkable corrosion resistance, demonstrated biocompatibility, and attractive mechanical properties. The incapacity of this substrate to degrade allows for the evaluation of HAp coating behavior by excluding the substrate dissolution, providing the background performance compared to biodegradable substrates [54,55]. The selection of these substrates provides a systematic evaluation of coating performance in different types of degradation environments, an assessment of the influence on alloying elements of the substrate on coating stability and biological activity, and an in-depth examination of both temporary and permanent implant applications. Furthermore, this comparison provides an essential overview of HAp coating performance across a broad range of available and potential biomaterial applications. Three different substrate materials were chosen to investigate the impact of substrate composition on coating morphology, biocompatibility, and antibacterial properties: MgZnMn alloy (Substrate I) was selected for its biodegradable properties and potential antibacterial effects; MgZnMnY alloy (Substrate II) was chosen to investigate the effect of yttrium addition on long-term biocompatibility; and Ti (Substrate III) was chosen as the clinical standard for implant materials to provide a reference benchmark for comparison as this substrate possesses the highest biocompatibility.

The substrates were cut into squares of 1 × 1 cm. Next, the samples were mechanically polished using #800 and #1200 SiC abrasive sandpaper. Next samples were washed 3 times by submersing them in ethanol for 10 min, under an ultrasound bath. After every step, the samples are rinsed with distilled water.

2.4.2. Deposition technique

The MAPLE system (Scheme 2) used to obtain the HAp coatings (from the Neocera company, Beltsville, MD, USA) includes the deposition chamber with a preliminary pump (DUO 20 M, Pfeiffer, Göttingen, Germany), a turbomolecular pump (TPU 170, Pfeiffer-Balzers, Göttingen, Germany), an optical system consisting of a focusing lens

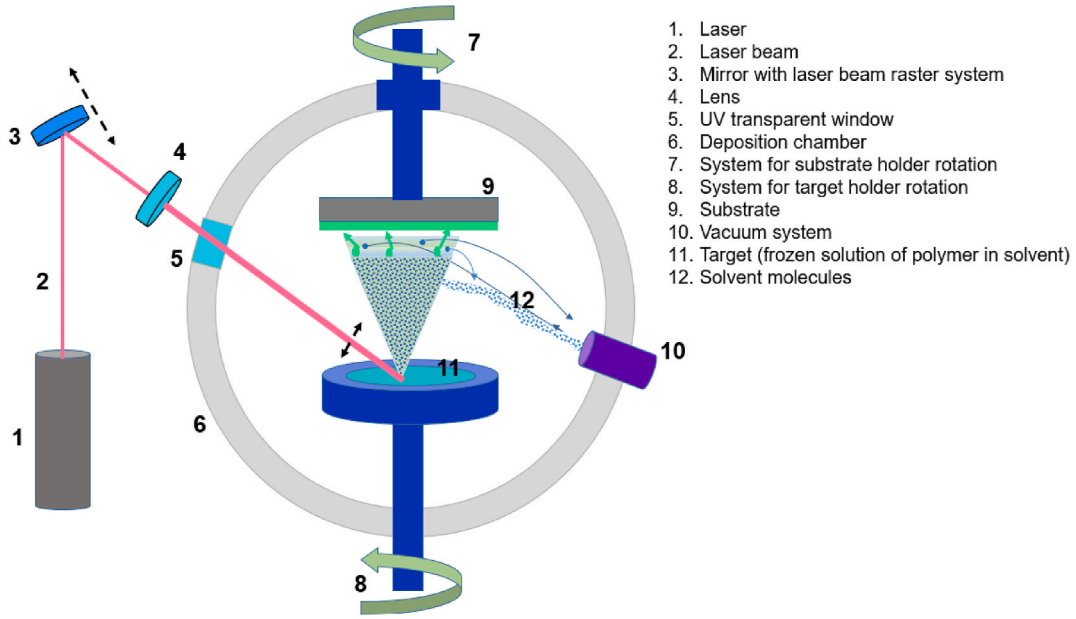

Scheme 2. Schematic representation of MAPLE deposition system.

(focal length of 100 mm) and two mirrors used to direct the laser beam to the target (at an incidence angle of ~45°).

For each deposition, a new target was prepared from HAp powder (each HAp powder type is described in Table 1), suspended in deionized water at a concentration of 6 % (wt/wt). This suspension was magnetically stirred for 2 h to obtain a homogeneous suspension/adequate dispersion of the suspension components. Then the suspension was poured into the holder, previously cooled to liquid nitrogen temperature, to obtain the solid target. Next, the solid target was placed in the deposition chamber. The target holder was rotated at 4°/s and positioned inside a tank connected to a cooling system that allowed a flow of liquid nitrogen to keep the target frozen throughout the experiment. The working pressure was in the range $6.9{\cdot}10^{-6}$ — $4.6{\cdot}10^{-5}$ mbar, while the distance between the target and the substrates (placed parallel to the target) was 28 mm or 23 mm. After reaching the pressure $4.6 \cdot 10^{-5}$ in the deposition chamber, the target was irradiated with a pulsed Nd: YAG laser (Surelite-II, Continuum), operated at the fourth harmonic, with 5–7 ns pulse duration and 10 Hz repetition rate. The laser spot was scanned on the target surface to avoid the formation of craters. In order to ensure a uniform coverage of the surfaces, the deposition parameters were chosen according to the type of material/HAp. The laser fluence was changed in the range of 0.895–1.186 J/cm^2 while the spot area was 0.51 mm^2. The process parameters for the deposition depend on the materials, since the obtained samples were compositionally different, and presented different concentrations. Thus, to obtain functional coatings, the deposition parameters, such as laser fluence and distance between the substrates and the target, were adapted to achieve coatings with functional thickness. Further, for some compositions where laser irradiation caused a larger plume, the parameters were modified to avoid the resputtering phenomenon of the deposition from the substrate. The exact parameters for each individual deposition are shown în Table 2.

Table 2
Target materials and deposition parameters.

Material	Laser fluence [J/cm^2]	Distance between the substrates and the target [mm]	Number of pulses
HAp_C	0.895	28	72000
HAp_Cu_1_C	1.178	23	39000
HAp_Cu_5_C	1.174	23	39000
HAp_Sr_1_C	1.019	28	72000
HAp_Sr_5_C	1.013	28	72000
HAp_Mg_1_C	0.913	23	42000
HAp_Mg_5_C	1.159	23	40200
HAp_S	1.000	28	72000
HAp_Cu_1_S	0.927	23	39000
HAp_Cu_5_S	0.912	23	39000
HAp_Sr_1_S	1.130	23	39000
HAp_Sr_5_S	1.070	23	39000
HAp_Mg_1_S	1.155	23	39000
HAp_Mg_5_S	1.186	23	39000

2.5. Characterization methods

2.5.1. X-ray diffraction (XRD)

Room temperature X-ray diffraction measurements were performed to investigate the phase composition and crystallinity. For this purpose, a Bruker D8 Advance diffractometer (Bruker AXS GmbH, Karlsruhe, Germany) using Ni-filtered Cu-Kα radiation (λ = 1.5418 Å) was used. The X-ray tube was operated at 40 kV and 40 mA. On the incident beam side motorized slits with 0.25 mm opening and a 2.5° soller slit were used and on the diffracted beam side motorized slits with 5 mm opening were mounted on LYNXEYE XE-T detector operated in 1D mode and high resolution option. The X-ray diffraction patterns were recorded in the 10–80° 2θ range, with a step size of 0.02° and a counting time of 0.2 s/step. Data reduction and search-and-match methods were carried out using HighScorePlus software version 3.0.e and the Crystallography Open Database database. Rietveld refinement was carried out sing a polynomial function for background approximation, a pseudo-Voigt function for peak profile, and a Caglioti function for peak width.

2.5.2. Fourier transform infrared spectroscopy (FT-IR)

The IR spectra of the obtained materials were acquired using a Thermo Scientific Nicolet iS50 spectrometer (Thermo Fischer Scientific, Waltham, MA, USA) to evaluate the functional groups present. The measurements were conducted at room temperature with a resolution of 4 cm^{-1}, and each sample underwent 64 scans across a wavenumber range of 4000 to 400 cm^{-1}. The spectrometer was connected to a data collection and processing device, utilizing the Omnic software (Thermo Nicolet, Version 8.2) to record and analyse the data. This setup allows for a comprehensive assessment of the functional groups, providing insights into the chemical characteristics of the materials. In order to determine the best compromise between the deposition efficiency and

compositional integrity of the deposited coatings, the surface distribution of the signal intensity of specific spectral markers was monitored, namely absorptions characteristic of the chemical functional groups of the deposited material. The FT-IR maps of the samples were recorded with a Nicolet iN10 MX (Nicolet, Waltham, MA, USA) FT-IR microscope. Each spectrum was the average of 32 scans at a resolution of 4 cm^{-1}. The resulting FTIR maps were converted to absorbance using Ominc Picta 8.2 software (Thermo Scientific, Waltham, MA, USA). About 250 spectra were analysed for each sample.

2.5.3. Morphological characteristics

2.5.3.1. Scanning Electron Microscopy (SEM). To examine the morphology of the obtained samples, a QUANTA INSPECT F50 scanning electron microscope (SEM) from Thermo Fisher in Eindhoven, The Netherlands, was utilized. This microscope is equipped with a field electron emission gun (FEG) that offers a resolution of 1.2 nm, along with an Energy Dispersive X-ray Spectroscopy (EDS) detector that has a resolution of 133 eV at the MnK line. The powder samples were mounted on a carbon-coated slide and placed into the analysis chamber for observation. This setup allows for detailed imaging and elemental analysis of the samples, providing valuable insights into their structural characteristics.

2.5.3.2. Profilometry. For roughness analyses, a Profilm3D (Filmetrics, San Diego, CA, USA) optical surface profilometer with composite WLI/PSI (White Light Interferometry/Phase Shifting Interferometry) was used. The measurements were performed using 10 × magnification lens and 4 × internal magnification. The optical surface profilometer uses the emitted light, focused on a determined height, to perform a non-contact vertical scan. The digital camera records the changes to the interference pattern during the scan and renders a 3D reconstruction of the surface. Equipment control, together with image acquisition, and analysis was performed with the help of Profilm Software (Filmetrics, San Diego, CA, USA).

2.5.3.3. Corrosion performance (in vitro bioactivity). To assess the long-term protective influence and bioactivity of HAp coatings, substrates were carefully evaluated following immersion in SBF solution prepared according to the Kokubo's protocol [56]. The immersion was conducted at 37 °C, with the solution renewed every 2–3 days to maintain stable ion concentrations. pH was measured using a Inolab Multi 9630 IDS pH meter (Xylem Analytics Germany Sales GmbH & Co., Weilheim Germany) to assure physiological conditions (pH 7.40 ± 0.05). For this experiment, samples were immersed in solutions for 7 days. To eliminate bound precipitates, each sample was rinsed with distilled water and dried at room temperature prior to analysis.

2.5.4. Biological evaluation

2.5.4.1. Antibacterial activity. The anti-adherent capacity of the samples developed in this research was determined by the colony-forming units/mL values (CFU/mL) [57–59]. Antibacterial activity has been assessed against *Staphylococcus aureus* ATCC 25923. Contaminants did not affect the experiment because all samples had been previously sterilized and exposed to UV light for 30 min on each side. Bacterial cell suspension (1.5×10^8 CFU/mL) has been prepared in a sterile physiological buffer (PBS) from fresh cultures (24 h). The quantitative evaluation of the antibiofilm activity of each sample was performed using a Nutrient broth: bacterial cell suspension ratio = 10:1, and the final density of 1.5×10^7 CFU/mL. The samples' anti-adherent capacity/biofilm formation was carried out following the approach reported in earlier studies [57–59] the CLSI standard [60]. The viable colony formation was measured in CFU (colony forming units)/mL. The CFU/mL values were expressed as the mean of the total number of colonies × 1/D (where D is the decimal dilution used to estimate the total number of colonies) [57–59]. The assays were carried out in three different experiments.

2.5.4.2. Biocompatibility assay. Considering the biological activity of the deposited samples on the metallic surfaces, the biocompatibility was investigated using XTT reagent (2,3-Bis-(2-Methoxy-4-Nitro-5-Sulfophenyl)-2H-Tetrazolium-5-Carboxanilide) according with the manufacturer protocol (CyQUANT™ XTT Cell Viability Assay Kit, Thermo Fischer Scientific, Waltham, MA, USA). In the assay kit, it is included also the Electron Coupling Reagent and XTT reagent. The XTT reagent is represented by a tetrazolium-based compound sensitive to the cellular redox potential. The water-soluble XTT compound is converted by the actively viable cells into an orange-coloured formazan product. The consistency and sensitivity of the analysis were substantially amplified when it was used with the Electron Coupling Reagent. The MC3T3 cell line was grown in DMEM medium (Sigma-Aldrich, Saint Luis, MO, USA) supplemented with 1 % antibiotics (penicillin and streptomycin) and 10 % fetal bovine serum, (Sigma-Aldrich, Saint Luis, MO, USA), which was changed twice a week. The cells were put in 96-well plates, at a density of 3000 cells/well in the presence of undoped and doped HA samples for 24h, and 48 h. Further, the control samples were represented only by cells cultivated in identical conditions, but without the presence of synthesized samples. Subsequently, 70 μL of XTT solution was added to the cells, followed by incubation at 37 °C for 4 h. After vigorous homogenization of formazan crystals, the absorbance was read at 450 nm using a spectrophotometer.

2.5.4.3. Statistical analysis. The data results were analysed using GraphPad Prism 10.4 from GraphPad Software (San Diego, California, USA). We compared the differences between groups using analysis of variance (ANOVA) and a multiple comparisons test. The differences between samples were considered statistically significant when the *p*-value was less than 0.05.

3. Results

In this investigation, samples are identified using a systematic nomenclature in which the calcium source is represented by C (eggshells) or S (mussel shells), doping ions can be identified (Cu, Mg, Sr), and concentrations are displayed as percentages (1 %, 5 %).

3.1. X-ray diffraction (XRD)

Fig. 1 presents XRD patterns of substituted and unsubstituted samples of HAp obtained using eggshells and mussel shells as CaO source. These samples were synthesized through the microwave-assisted hydrothermal treatment process. XRD analysis confirmed the successful synthesis of both undoped and doped HAp samples, using either eggshells or mussel shells as CaO precursors.

The diffraction data obtained corresponding to the undoped sample, which used eggshells as CaO source demonstrated the successful synthesis of HAp (COD # 96-900-2215). Furthermore, in the same figure, a small amount of $Ca(OH)_2$ secondary phase was also detected (COD # 96-100-0046). Similarly, the diffraction pattern of the sample using mussel shells as CaO precursor also confirmed the synthesis of HAp (COD # 96-900-2214). Likewise, the diffraction data of all doped samples confirmed the successful synthesis of HAp, consistent with the standard data. All obtained samples presented a hexagonal crystallization system with a $P6_3/m$ space group. For the samples derived from eggshells, the principal and sharp diffraction peaks were identified at 2θ values of 25.82, 31.69, 46.71, and 49.42, corresponding to (0 0 2), (2 1 1), (2 2 2), and (2 1 3) Miller indices. Similarly, the samples derived from mussel shells exhibited broader diffraction peaks at 2θ values of 25.81, 29.21, 31.99, 46.76, and 49.39 corresponding to (0 0 2), (2 1 0), (2 1 1), (2 2 2) and (2 1 3) diffraction planes. Moreover, according to the diffraction patterns

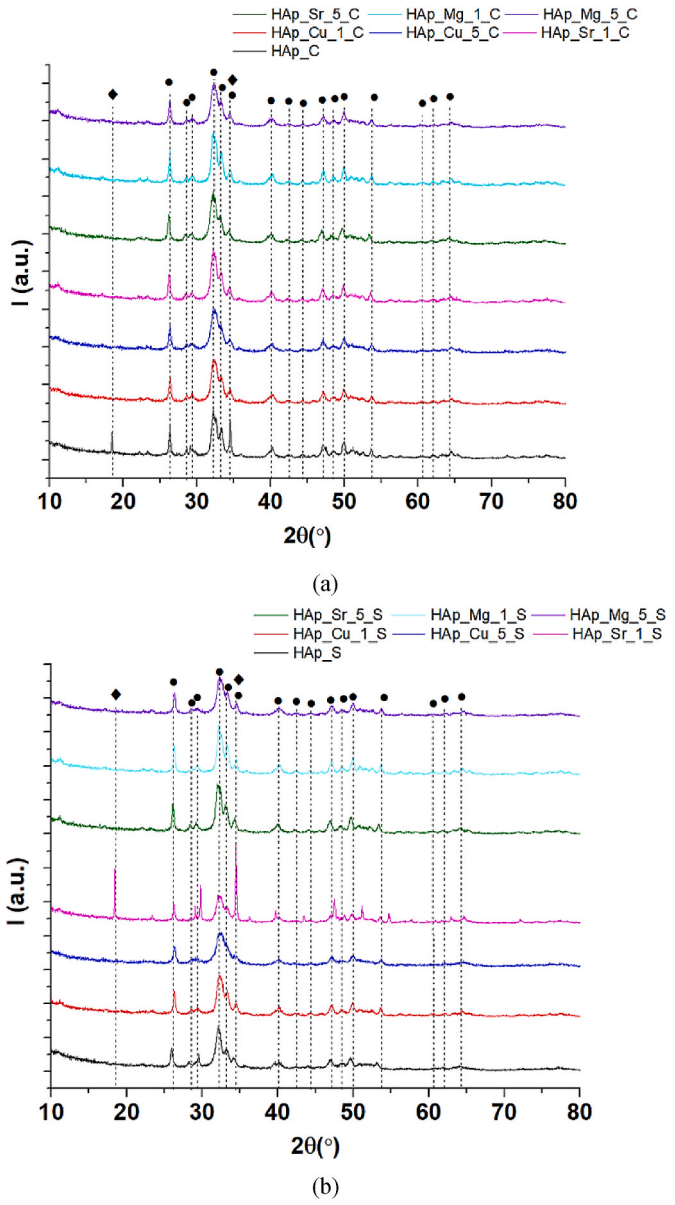

Fig. 1. XRD patterns of the synthesized samples, obtained from (**a**) eggshells and (b)mussel shells. Cu, Mg, Sr indicate substituting ions; and 1, 5 represent concentrations (%). ◆ —$Ca(OH)_2$, ●— $Ca_{10}(PO_4)_6(OH)_2$.

of Sr, Mg, and Cu – substituted HAp, the incorporation of doping ions was highlighted into the HAp lattice without altering its chemical structure [61,62]. For Cu-doped HAp, the substitution of Cu^{2+} ions led to a decrease in crystallinity, which can be observed through lower peak intensities and minor deviations in the XRD pattern [63]. The incorporation of Mg^{2+} ions into the HAp structure has been also demonstrated by the peak shift in all obtained samples. This shift indicates structural modifications within the HAp lattice due to the successful integration of substituted ions [11].

Furthermore, Sr substitution led to the apparition of broader peaks on the diffraction patterns, thus, a reduced crystallinity. As the Sr concentration increases, the peak intensities decrease, and a slight shift in peak positions is observed, confirming structural changes and ion incorporation. Considering this, the incorporation of Sr, Mg, and Cu ions into the HAp structure influences its crystallinity and diffraction patterns, confirming successful doping and structural adjustments. Furthermore, by evaluating the average crystallite size from Table 3, in accordance with Scherrer formula, important modifications can be observed, confirming the influence of the substituting ion.

The effect of the dopants and the HAp source (eggshells or mussel shells) were assessed by the determination of the unit cell parameters and crystallite size (Table 3). The unsubstituted HAp, eggshell-derived (C) samples have a a = 9.430 Å, c = 6.881 Å, volume $V \approx 529.9$ Å^3, and D ≈ 13.6 nm, whereas mussel-shell (S) HAp has smaller a = 9.393 Å but larger c = 6.916 Å ($V \approx 528.4$ Å^3) and much smaller D ≈ 8.1 nm. This difference in raw precursors yields smaller, more highly c-axis–extended crystals from mussel shells than from eggshells [64].

In eggshell-derived HAp (C), 1 % Cu causes a slight increase in *a* (9.430 → 9.434 Å) and a decrease in *c* (6.881 → 6.879 Å) and volume (529.9 → 530.3 Å^3), while 5 % Cu reduces both *a* (9.428 Å) and *c* (6.870 Å) relative to unsubstituted HAp. The net effect at higher Cu is a small contraction of the unit cell. In mussel-derived HAp (S), 1 % Cu substitution causes an increase in *a* parameter (9.393 → 9.435 Å) and a decrease in *c* (6.916 → 6.885 Å), giving a large *V* increase (528.4 → 530.8 Å^3), whereas 5 % Cu maintains *a* at 9.435 Å but further contracts *c* to 6.869 Å (volume back to ~529.4 Å^3). Overall, low Cu often slightly expands *a* but higher Cu shrinks both axes. Crystallite size <*D*> decreases with Cu content in both sources: eggshell HAp decreases from 13.6 nm to 8.4 nm at 5 % Cu, and mussel HAp first increases (8.1 → 11.5 nm at 1 % Cu) then decreases to 6.6 nm at 5 % Cu. These trends are in agreement with reported literature results: Cu^{2+} (ionic radius ~0.73 Å for sixfold coordination) is smaller than Ca^{2+} (~1.00 Å), and, thus, substituting Ca by Cu shrinks the lattice [65].

Strontium ions (Sr^{2+}) are larger (~1.18 Å) than Ca^{2+} [66]. In eggshell HAp, 1 % Sr doping results in almost unchanged *a* (9.430 → 9.429 Å) but slightly larger *c* (6.881 → 6.885 Å) and volume (529.9 → 530.2 Å^3). At 5 % Sr, both *a* and *c* rise (9.462 Å and 6.908 Å), leading to a large increase of the *V* to 535.6 Å^3. Mussel HAp shows

Table 3
Unit cell parameters, average crystallite size of the substituted and unsubstituted HAp samples, and agreement indices of Rietveld refinement.

Sample	Unit cell parameters				Crystallite size	Agreement indices			
	a [Å]	b [Å]	c [Å]	V [Å^3]	<D> [nm]	R_{exp}	R_p	WR_p	χ^2
HAp_C	9.430 ± 0.001	9.430 ± 0.001	6.881 ± 0.001	529.917	13.63 ± 1.41	18.900	12.471	16.783	0.788
HAp_Cu_1_C	9.434 ± 0.002	9.434 ± 0.002	6.879 ± 0.002	530.285	10.03 ± 1.19	18.361	12.926	16.88	0.845
HAp_Cu_5_C	9.428 ± 0.003	9.428 ± 0.003	6.870 ± 0.002	528.888	8.38 ± 0.82	16.523	11.111	14.593	0.780
HAp_Sr_1_C	9.429 ± 0.002	9.429 ± 0.002	6.885 ± 0.002	530.173	10.94 ± 1.24	18.427	13.026	17.073	0.858
HAp_Sr_5_C	9.462 ± 0.002	9.462 ± 0.002	6.908 ± 0.002	535.600	9.57 ± 1.09	18.120	12.935	16.845	0.864
HAp_Mg_1_C	9.425 ± 0.002	9.425 ± 0.002	6.878 ± 0.001	529.112	13.09 ± 1.42	18.725	13.698	17.882	0.912
HAp_Mg_5_C	9.430 ± 0.003	9.430 ± 0.003	6.874 ± 0.002	529.390	9.37 ± 1.28	18.622	13.272	17.268	0.859
HAp_S	9.393 ± 0.003	9.393 ± 0.003	6.916 ± 0.003	528.4388	8.05 ± 1.73	17.776	13.580	17.803	1.003
HAp_Cu_1_S	9.435 ± 0.002	9.435 ± 0.002	6.885 ± 0.002	530.7686	11.53 ± 0.9	18.601	12.740	16.700	0.806
HAp_Cu_5_S	9.435 ± 0.005	9.435 ± 0.005	6.869 ± 0.004	529.4296	6.63 ± 0.98	16.65	11.245	14.621	0.770
HAp_Sr_1_S	9.428 ± 0.002	9.428 ± 0.002	6.883 ± 0.002	529.8269	10.04 ± 1.07	19.119	16.286	23.815	1.551
HAp_Sr_5_S	9.452 ± 0.002	9.452 ± 0.002	6.906 ± 0.001	534.3065	11.75 ± 1.3	18.050	13.004	16.976	0.884
HAp_Mg_1_S	9.428 ± 0.001	9.428 ± 0.001	6.882 ± 0.001	529.7117	14.18 ± 1.32	19.060	13.355	17.635	0.856
HAp_Mg_5_S	9.431 ± 0.003	9.431 ± 0.003	6.878 ± 0.002	529.8219	9.47 ± 1.22	18.776	13.290	17.296	0.848

similar trends: 1 % Sr increases *a* (9.393 → 9.428 Å) and slightly reduces *c*, while 5 % Sr increases *a* further (9.452 Å) and *c* (6.906 Å), giving $V = 534.3$ Å^3 (much higher than 528.4). Thus Sr doping expands the unit cell (especially *a* and *V*), consistent with the larger Sr radius. Literature confirms this linear expansion: e.g. Sr substitution in HAp linearly increases a, c, and volume [67]. Crystallite sizes <*D*> generally decrease in eggshell samples (from 13.6 nm down to 9.6–10.9 nm as Sr increases). In mussel samples, however, D increases (8.1 → 11.8 nm at 5 % Sr), suggesting that Sr may promote crystal growth in that system.

Magnesium (Mg^{2+}) has ionic radius ~0.72 Å, smaller than Ca^{2+}. Eggshell HAp shows slight contraction at 1 % Mg ($a = 9.430 \rightarrow 9.425$ Å, $c = 6.881 \rightarrow 6.878$ Å, $V = 529.9 \rightarrow 529.1$ Å^3) and very small changes at 5 % (a = 9.430 Å, c = 6.874 Å). Volume is essentially unchanged or slightly reduced. Crystallite D decreases slightly (13.6 → 13.1 nm at 1 % Mg, then to 9.4 nm at 5 %). Mussel HAp trends were unexpected: both *a* and *V* increased slightly ($a = 9.393 \rightarrow 9.428$–$9.431$ Å, $V \approx 529.7$ Å^3) while *c* decreased. This might reflect measurement or structural differences, but overall Mg doping causes slight lattice contraction or distortion. Rietveld analysis in one study similarly noted that Mg^{2+} incorporation causes a "slight lattice parameter shortening" in Hap [68]. Notably, Mg-doped samples often had larger D than base HAp in mussel series (8.1 → 14.2 nm at 1 % Mg) before decreasing at higher Mg content, implying that low-level Mg may encourage crystal growth or coarsening, whereas higher Mg leads to decreasing crystallization rate.

Shannon radii explain these trends. In 6–7 coordination (as in HAp Ca sites), Ca^{2+} is approximatively 1.00–1.06 Å. Sr^{2+} is larger (~1.18 Å), while Cu^{2+} and Mg^{2+} are smaller (0.72–0.73 Å). Thus, substituting Ca with Sr^{2+} *expands* the lattice, whereas Cu^{2+} or Mg^{2+} *shrink* it. Indeed, Noori et al. [65] noted that "when copper substitutes calcium, the smaller ionic radius of Cu^{2+} (0.73 Å) compared to Ca^{2+} (1.00 Å) causes apatite structural shrinkage". Similarly, Baldassarre et al. [67] observed a linear increase in all lattice parameters (a, c, V) with Sr content, since "Sr–Ca substitution leads to a lattice expansion (due to larger Sr atom) … shifting peaks to lower angles".

HAp has two Ca sites: Ca1 (9-coord) and Ca2 (7-coord). Larger cations like Sr^{2+} tend to occupy the more spacious Ca1 sites at low doping, moving into Ca2 at higher loadings. Smaller cations (Mg^{2+}, Cu^{2+}) more easily fit into the tighter Ca2 site or cause local distortions.

3.2. Fourier-Transform Infrared Spectroscopy (FT-IR)

Fourier transform infrared (FT-IR) spectra of all obtained samples is presented in Fig. 2. After analysing the obtained materials, the principal functional groups associated with HAp were identified in both substituted and unsubstituted samples. According to the literature, the bands at 559-600 cm^{-1} correspond to the υ1 symmetric stretching of PO_4^{3-}, while those at 1018-1081 cm^{-1} correspond to the υ3 asymmetric stretching of PO_4^{3-} groups. Additionally, in all samples, the υ2 vibration bands could be identified, as well as the υ3 vibration bands of CO_3^{2-} at 1413-1420 cm^{-1} and 1451-1537 cm^{-1}. The broad peaks between 1640 and 1651 cm^{-1} also confirmed the presence of OH-bending vibrations, confirming the existence of adsorbed water in the samples. Furthermore, the stretching vibration of OH, specific to HAp, can be identified around 3367-3567 cm^{-1} [69,70]. All ion-substituted samples presented the characteristic functional groups of HAp. The addition of doping ions led to an increase in peak intensity, corresponding with the increase of ion concentration. While the PO_4^{3-} ion bands were very similar with undoped samples, the OH group bands broadened, indicating a decrease in the number of hydroxyl groups. The stretching vibration of OH between 3367 and 3567 cm^{-1} also broadened, suggesting that the concentration of OH groups in the OH channel was unaffected by doping, though the presence of substituents in the surrounding area reduced hydroxyl group vibrations [71–75]. Further, ion substitution into the HAp lattice did not alter the functional groups, but a slight decrease in OH group intensity was observed [76]. This reduction is attributed to the substitution of Ca^{2+} within the HAp structure, consistent with the XRD results, and was

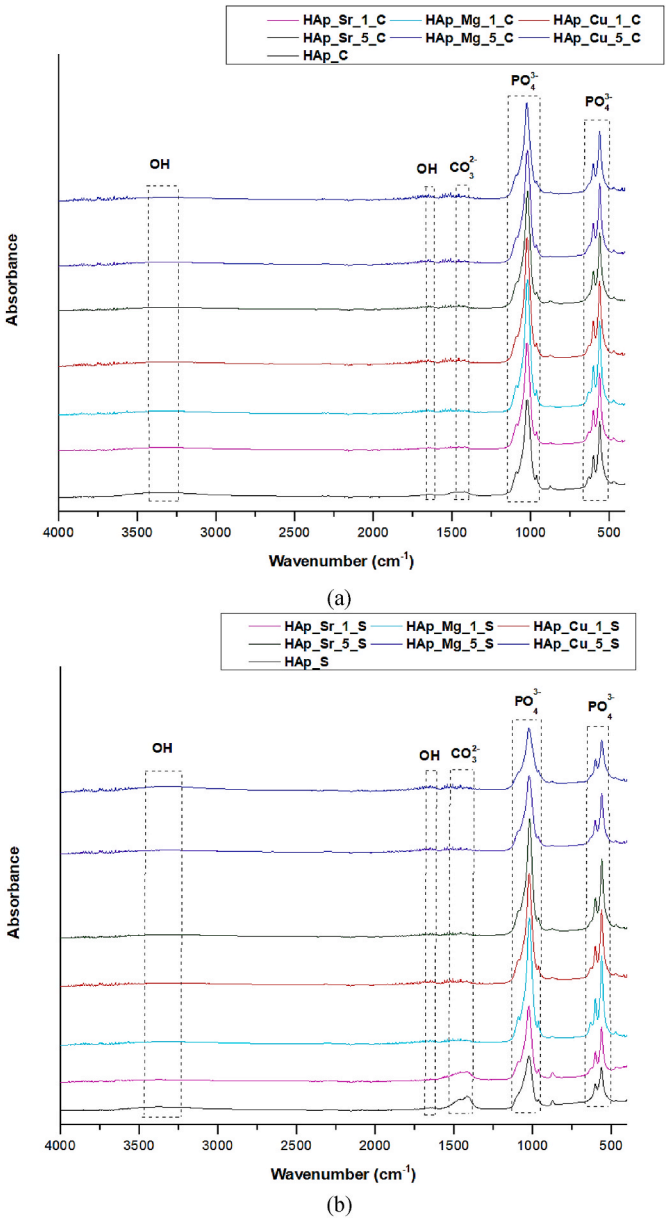

Fig. 2. FTIR spectrum of the synthesized samples, obtained from eggshells (**a**) and mussel shells (b). Cu, Mg, Sr indicate substituting ions; and 1, 5 represent concentrations (%).

reported previously in literature [77,78].

To analyse and compare how chemical compounds of the synthesized samples were distributed spatially within the deposited coatings on the substrates, FT-IR spectroscopic imaging was performed. The colour scale of the maps obtained in this study was adjusted from a peak height of 0–0.1 to perform image analysis. Through the resulted imaging data, the distribution of selected compounds between the samples could be observed, as shown in Figs. 3 and 4. The analysed region is generated by the stretching vibrations of phosphate region of HAps, between 1100 and 1033 cm^{-1} [79,80]. The colour distribution within images from yellow to orange and red represent the strongest peak intensity of the detected intensity range. The values of correlation maps confirmed a considerate homogeneity of the amorphous material on the surface. In this direction, the obtained spectra obtained from the spectroscopic imaging of the samples displayed the characteristic bands related to the phosphate species [81]. For all samples, it could be observed an increased peak intensity on the scratch marks on all three substrates or

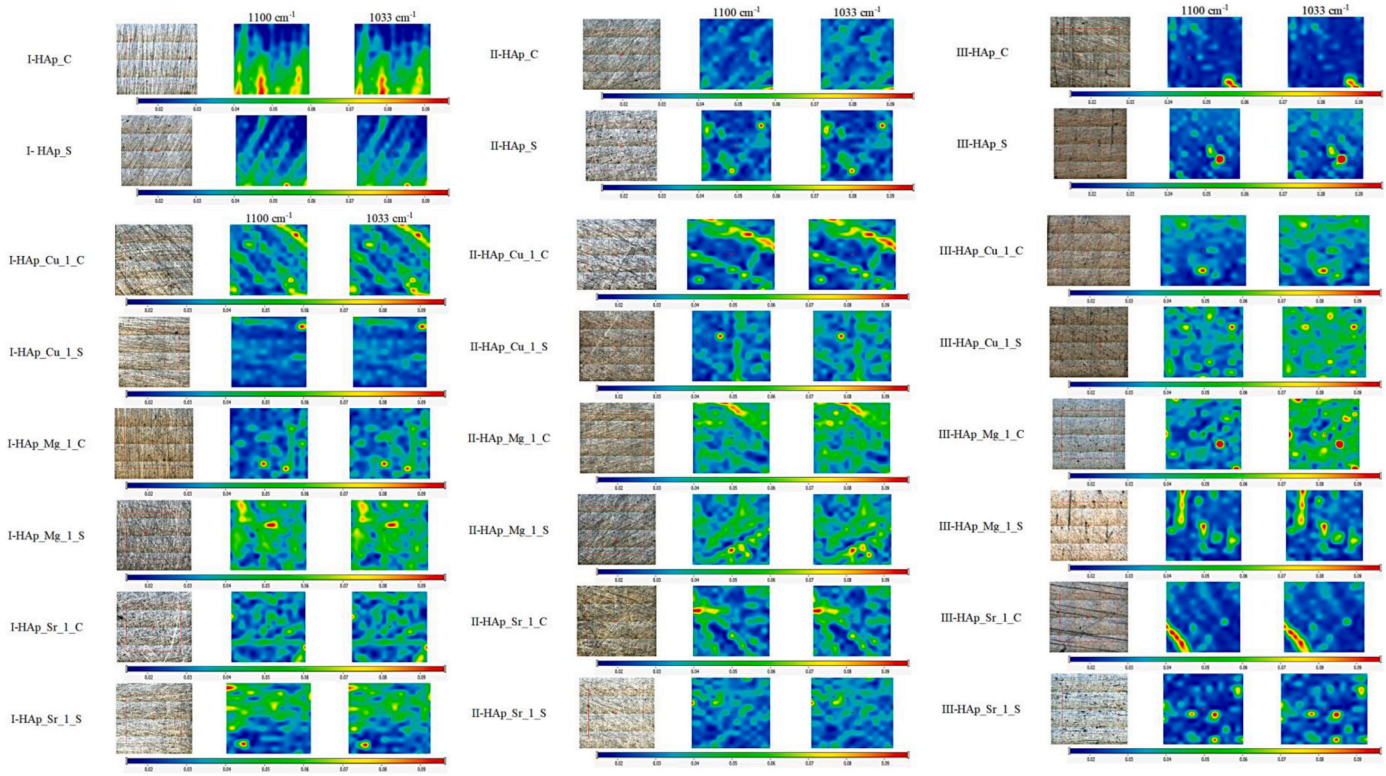

Fig. 3. FT-IR images of substituted with 1 % doping ions and unsubstituted HAp deposited films. The images are generated by ratioing the band area of the PO_4^{3-} stretch between 1100 and 1033 cm^{-1}.

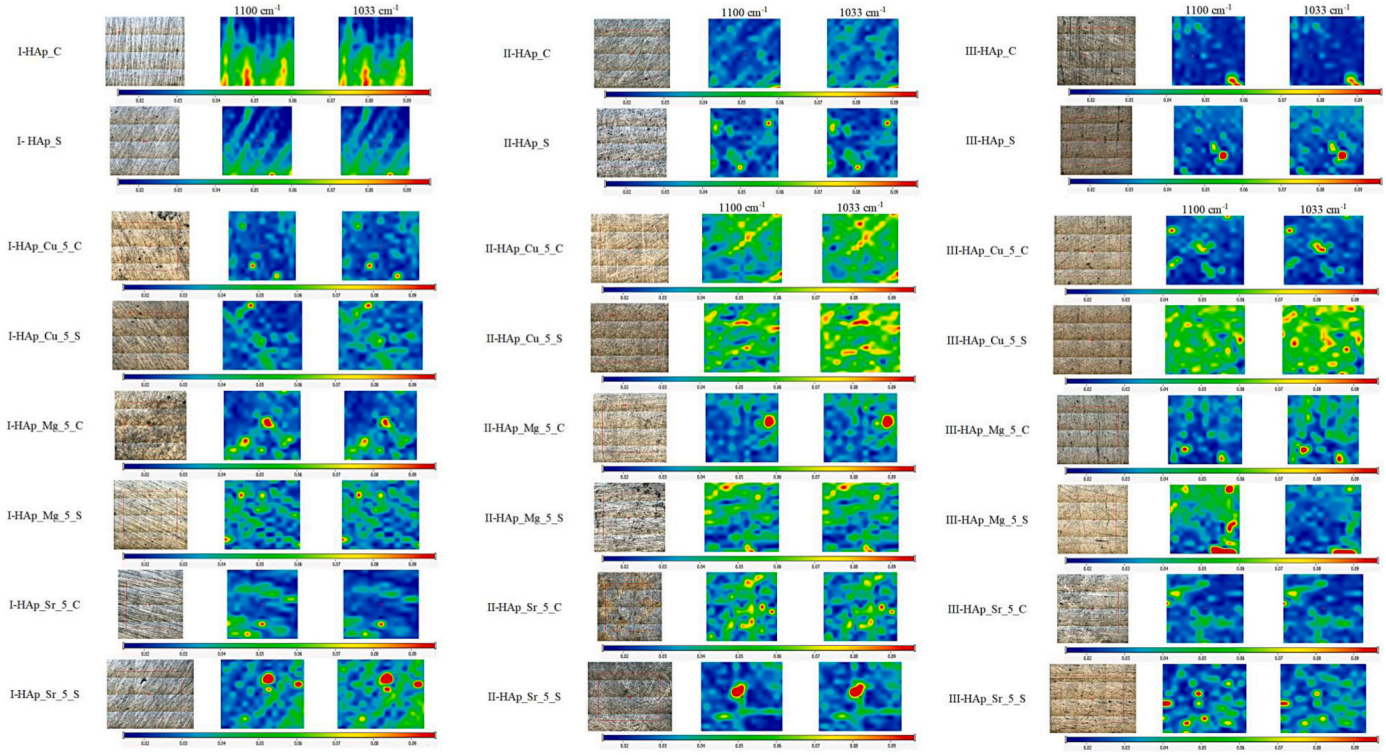

Fig. 4. FT-IR images of substituted with 1 % doping ions and unsubstituted HAp deposited films. The images are generated by ratioing the band area of the PO_4^{3-} stretch between 1100 and 1033 cm^{-1}.

defect sites.

3.3. Morphological characteristics

3.3.1. Particle morphology

The morpho-structural properties of the samples were assessed with the aid of Scanning Electron Microscopy (SEM), as shown in Figs. 5 and 6. The SEM micrographs display elongated particle shapes for all synthesized samples. Considering doping ions and concentration, while the doping concentration increased, the nanoparticles tended to agglomerate. Additionally, the morphology of the nanoparticles changed with increasing doping concentrations. On the other side, depending on the CaO precursor source, the HAp derived from eggshells had sizes between 3 and 25 nm, whereas HAp from mussel shells had sizes between 4 and 29 nm.

3.3.2. Coatings morphology

The coatings on the substrates are also presented in Figs. 7 and 8. The SEM micrographs exhibit distinct surface morphologies and the textures very based on the substrate material applied. In samples produced from eggshells, the resulting coatings exhibited increased porosity, while the coatings derived from mussel shells showed a smooth and dense appearance. Additionally, depending on the type of substrate, the coated Titanium plates illustrated an increased smoothness and improved uniformity of the deposited samples. Additionally, this specific substrate showed fewer abrasion marks caused by the polishing process used in preparing the plates. The influence of substituting ion concentration has also been investigated in Fig. 7. It is evident that as the concentration of doping ions increases, the fractures on the coating surfaces become more noticeable. These changes in microstructure can affect the physical, chemical, and mechanical characteristics of the deposited films, thereby influencing their effectiveness in biomedical applications. Table 4 shows a comprehensive comparison of the coating shape and characteristics among the three substrate materials. Regardless of the source of the precursor, Substrate I consistently achieved the most porous coatings, the samples obtained from eggshells displaying the highest levels of porosity. This high porosity could be beneficial for increased bioactivity and drug delivery applications. Substrate II (MgZnMnY) exhibited intermediate characteristics, including moderate porosity and good coating uniformity, indicating balanced properties for biomedical applications. Substrate III (Ti) produced the most uniform coatings with high surface coverage and low porosity, demonstrating its superior surface energy and proven biocompatibility profile.

3.3.3. Profilometry

Profilometry experiments were performed on 5 % doped samples to evaluate surface properties under maximum dopant loading. This concentration was selected as it represents the maximum concentration of dopant incorporation while maintaining the structural integrity of the HAp lattice, as proven by XRD analysis. This concentration represents the optimal balance between significant surface modification and maintained structural integrity, providing the most pronounced topographical differences necessary for optimum substrate comparison and biological correlation analysis.

Images from Fig. 9 show the topographic profile present on the surface of the deposited samples. These samples were investigated and mapped by optical profilometry measurements through composite WLI/PSI technique using a Filmetrics Profilm 3D optical profiler. To quantify the surface texture or roughness of the surface we compared the values of the root mean square roughness (Sq), as seen in Fig. 10. Rq was evaluated according to the ISO 25178 standard. While analyzing the values, differences in roughness between the samples are observed. It can be seen that the films incorporating Cu, regardless of the group, have lower roughness than the other films, indicating a smoother surface. Additionally, the coated Ti plates illustrated an increased smoothness and improved uniformity of the deposited samples, in concordance with the results obtained through SEM.

An extensive characterization of samples roughness and uniformity was performed (Table 5). Valley depth (Sv) indicates how deep surface features extend. Maximum peak-to-valley height (St) reflects extreme surface variations. Arithmetic mean height (Sa) & Sq represent overall surface roughness. C_I yields the most pronounced microstructure (deepest features, highest relief). At the same time, C_II produces the most controlled and uniform surfaces, being best for reproducibility. C_III has divergent results depending on the dopant, with Sr increasing roughness, Cu lowering it. Moreover, S_I produces the roughest, most topographically varied surfaces. On the other side, S_II smooths the surfaces appreciably while retaining some pronounced features. S_III delivers the flattest and most uniform coatings of the S-series.

C-series — the samples prepared by using eggshells as CaO precursors — generally shows greater variability in roughness metrics, particularly in Group III. S-series — the samples prepared by using mussel shells as CaO precursors — tends to have higher roughness in Group II for most parameters. Group III marks the most significant distinction between the two series, with C-series typically rougher.

Implant surface roughness is a critical factor influencing the biological response at the tissue–implant interface. Moderate roughness, particularly an Sa in the range of approximately 0.2–0.5 μm, has been shown to promote optimal cell adhesion and proliferation. Additionally, micro- and nano-scale surface features enhance protein adsorption, which is essential for the initial stages of osseointegration. Effective bone integration also benefits from a well-defined topography, with St values exceeding 3 μm and Sv values greater than 1.5 μm, providing mechanical interlocking and increased surface area for cell interaction. Therefore, ideal bioactive coatings should exhibit moderate Sa and Sq values (typically around 0.2–0.4 μm), along with sufficient St and Sv to support cellular responses, while avoiding surfaces that are either excessively smooth, potentially leading to poor bone bonding, or overly rough, which may trigger inflammation or particle release.

Based on the comparative analysis of surface roughness parameters, the most promising coating system for bioactive implant applications is the Sr-doped HAp in Group II of the S-series, which demonstrated the most favorable combination of surface topography and roughness values. This system exhibited peak and valley characteristics conducive to cell adhesion and osteointegration, further enhanced by the known biological benefits of Sr in bone regeneration. The second most possibly effective system was the Mg-doped HAp, also from Group II of the S-series, which may have strong bioactivity supported by optimal surface roughness and a high St. In contrast, Cu-doped coatings, across all groups and series, exhibited surfaces that were comparatively too smooth to effectively support bone integration (Table 6).

The S-series coatings provide a more consistent and biofunctionally favorable surface roughness profile compared to the C-series. While the C-series may produce rougher or more complex surfaces, the S-series strikes a better balance between topographical features and uniformity.

3.3.4. Corrosion performance (in vitro bioactivity)

The comprehensive analysis of HAp-coated substrates through long-term SBF immersion testing provides detailed information about the degradation mechanisms and protective capacity of these biodegradable coating systems. The studies were conducted out on 5 % doped and undoped samples to assess surface properties over maximum dopant loading, as this represents the ideal balance between significant surface modification and structural integrity. The findings from experiments show that corrosion behaviour, surface morphological evolution, and bioactivity responses varies depending on substrate composition, coating dopant chemistry, and precursor material selection.

The precursor source selection had important influence on the corrosion resistance of the developed coatings, especially eggshell-derived HAp coatings, providing better corrosion resistance than mussel shell-derived samples. As shown in Table 7, the addition of substituting ions has different effects on the corrosion performance of

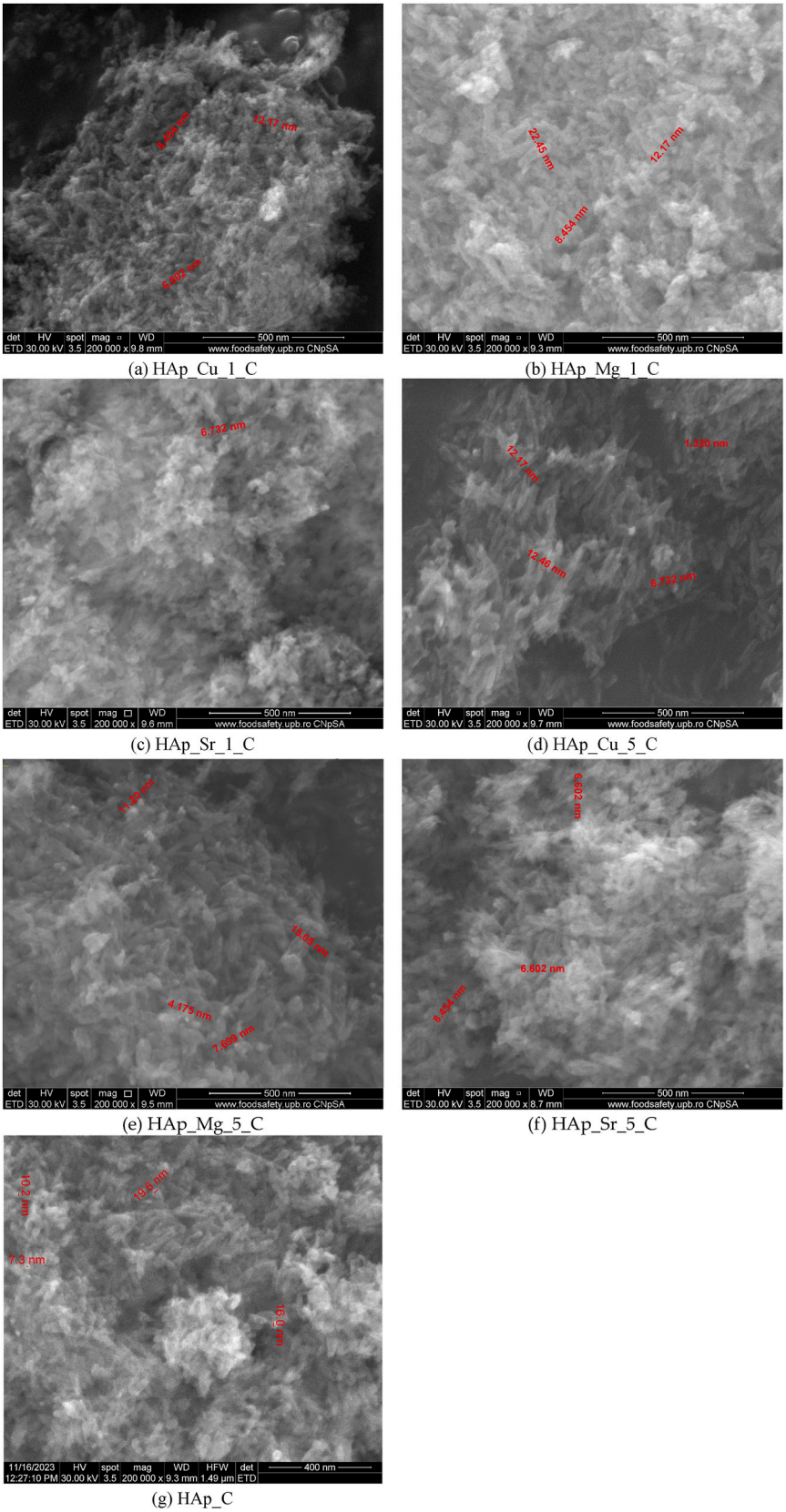

Fig. 5. SEM micrographs of the synthesized doped and undoped HAp samples obtained from eggshells: (a) HAp_Cu_1_C: 1 % Cu-doped HAp; (b) HAp_Mg_1_C: 1 % Mg-doped HAp; (c) HAp_Sr_1_C: 1 % Sr-doped HAp; (d) HAp_Cu_5_C: 5 % Cu-doped HAp; (e) HAp_Mg_5_C: 5 % Mg-doped HAp; (f) HAp_Sr_5_C: 5 % Sr-doped HAp; (g) HAp_C: undoped HAp. All samples derived from eggshells as CaO source.

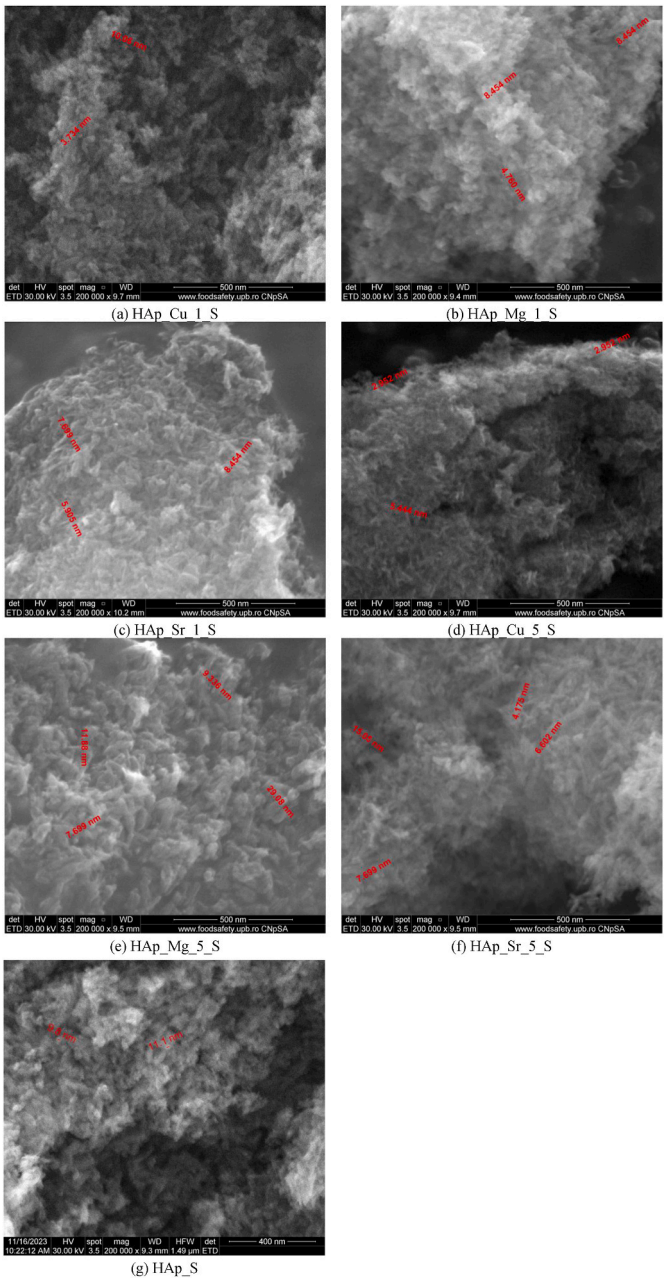

Fig. 6. SEM micrographs of the synthesized doped and undoped HAp samples obtained from mussel shells. (a) HAp_Cu_1_S: 1 % Cu-doped HAp; (b) HAp_Mg_1_S: 1 % Mg-doped HAp; (c) HAp_Sr_1_S: 1 % Sr-doped HAp; (d) HAp_Cu_5_S: 5 % Cu-doped HAp; (e) HAp_Mg_5_S: 5 % Mg-doped HAp; (f) HAp_Sr_5_S: 5 % Sr-doped HAp; (g) HAp_S: undoped HAp. All samples derived from mussel shells as CaO source.

the coatings. In this regard, Cu^{2+} doping has a significant influence on corrosion resistance. The 5 % Cu-doped eggshell-derived coating on Substrate I had the lowest corrosion rate of −0.634 mm/year, a significant improvement over the undoped sample. Further, the negative corrosion rates indicate active biomineralization processes in which Cu ions could stimulate HAp synthesis and increase CaP precipitation. Mg substitution provides intermediate performance, with significant differences in corrosion performance depending on concentration and substrate. While 5 % Mg doping in eggshell samples improves corrosion resistance, the same dosage in mussel shell samples increases corrosion rates. This result is consistent with the crystallite size differences observed in the structural study, which showed that Mg^{2+} doping influenced crystal development distinctively according to the precursor source. At the same time, Sr^{2+} doping presents moderate corrosion resistance in all developed samples. Furthermore, the negative values suggest rapid but uncontrolled apatite formation, promoting enhanced biological integration through increased ion exchange.

The substrate material has significant effect on corrosion behavior, particularly on Substrate III (Ti) consistently providing more accurate corrosion resistance of less than −0.5 mm/year across all coating samples. This excellent performance generates controlled biomineralization environments by using smooth, dense coatings that promote consistent apatite nucleation while reducing uncontrolled dissolution. The superior surface coatings shown in SEM micrographs (Fig. 11) are connected to decreased electrolyte infiltration and improved resistance characteristics, which promote systematic HAp production on Ti substrates. MgZnMnY substrates (Substrate II) possess moderate corrosion resistance, promoting stable HAp production via controlled ion release processes. The moderate performance shows that optimal conditions for biological integration emerge as corrosion rates enhance biomineralization while preserving coating integrity. In contrast, MgZnMn substrates (Substrate I) exhibit variable behavior, with increased porosity allowing for faster apatite precipitation but potentially compromising long-term coating stability. This variation shows substrate-dependent biomineralization kinetics, which necessitate careful modification for medical applications.

Furthermore, from Fig. 11 significant correlations can be observed between coating morphology and biomineralization potential, indicating a direct connection between porosity and biological activity. Considering this, higher porosity coatings on MgZnMn substrates exhibit bigger corrosion rates, which could promote improved biological fluid absorption and subsequent apatite formation, whereas dense coatings on Ti provide controlled corrosion rate. The appearance of defects and fractures in doped samples is associated with localized biomineralization spots that may act as nucleation centers for bone integration. The variation in results demonstrates substrate-dependent biomineralization dynamics, which necessitate specific adjustments for particular applications.

pH measurements performed after 168-h immersion tests (Fig. 12) show controlled dissolution behavior with values ranging from 7.4 to 9.5, suggesting stable chemical environments suitable for physiological apatite formation. The consistent pH profiles indicate that coatings maintain biomineralization-friendly parameters without quick degradation. Considering these results, titanium (Substrate III) demonstrated particularly stable pH maintenance due to enhanced coating integrity and reduced ion leaching. Moreover, Hernández-Cortés [82] mentioned that pH values > 7, such as those generated in the SBF for immersion more than 168 h, allow the undetached or undissolved species from the substrate to be more stable, offering an effective barrier against corrosion.

These corrosion characteristics have important medical applications. Cu-doped samples have the potential to combine corrosion protection with antimicrobial activity, whereas Sr-doped coatings have acceptable corrosion rates as well as known bone-forming properties that promote osseointegration. The consistent performance of Ti substrates across all coating samples indicates that surface preparation and substrate selection are essential variables in obtaining effective corrosion protection and regulated biomineralization in biomedical applications.

3.4. Biological evaluation

Firstly, the biological assessments consist of anti-adherent capacity evaluation. Biofilms are aggregates formed by microorganisms as a protective survival mode to adapt to their surroundings. They can be resistant to antimicrobial agents and host immune responses due to chemical or physical diffusion barriers, modified nutrient environments, growth rate suppression within biofilms, and genetic adaptation of cells. With the extensive use of medical devices, medical device-associated

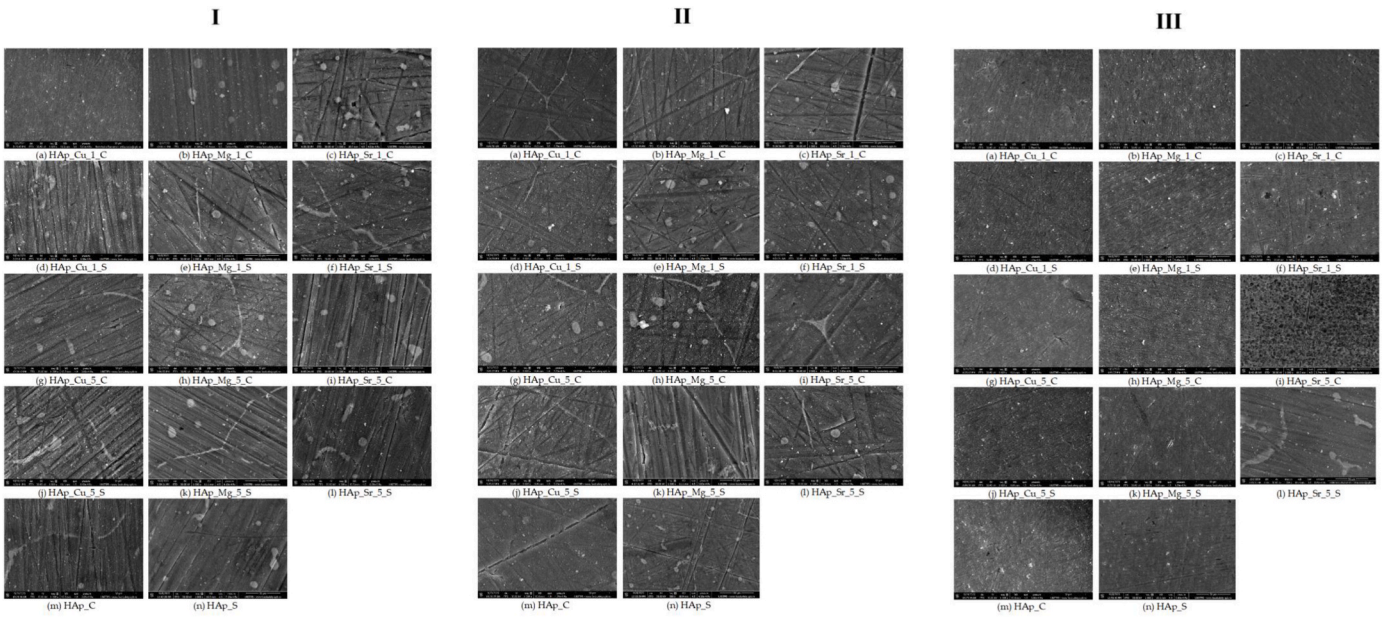

Fig. 7. SEM micrographs of deposited samples at 1000X magnification: substrates are coded as follows: substrate I – MgZnMn (Mn 0.62 Zn 4.3), substrate II - MgZnMnY (Zn 7.1 Mn 1.17 Y 1.2) and substrate III – Titanium. Scale bar of micrographs: 50 μm. Cu, Mg, Sr indicate substituting ions; 1, 5 represent concentrations (%).

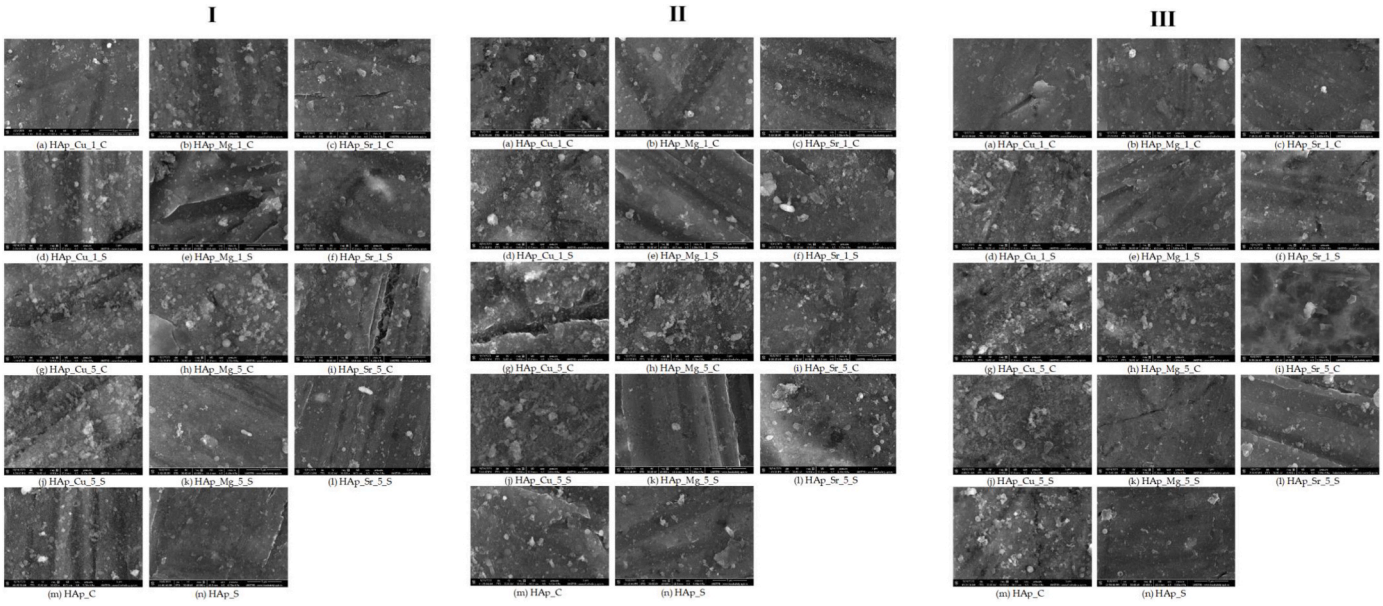

Fig. 8. SEM micrographs of deposited samples at 10,000X magnification: substrates are coded as follows: substrate I – MgZnMn (Mn 0.62 Zn 4.3), substrate II - MgZnMnY (Zn 7.1 Mn 1.17 Y 1.2) and substrate III – Titanium. Scale bar of micrographs: 5 μm. Cu, Mg, Sr indicate substituting ions; 1, 5 represent concentrations (%).

Table 4
Comparison of coatings morphologies.

Substrate	Surface Texture	Porosity	Coating Uniformity
I (MgZnMn)	Rough	High	Moderate
II (MgZnMnY)	Intermediate	Moderate	Good
III (Titanium)	Smooth	Low	Excellent

biofilms continue to pose a severe hazard to human health. These biofilms have become the most important cause of nosocomial infections [83]. In this direction, *S. aureus* shown an increased potential to form biofilms as these bacteria may remain quiescent for years without producing any symptoms [84]. These bacteria can attach to implant surfaces, multiply, and build protective polymeric biofilms difficult to remove than planktonic bacteria in the body, even with antibiotic treatment. Furthermore, biofilm growth on implants may inhibit host cell adhesion to the implant surface, resulting in poor osseointegration and implant failure [85]. In this regard, the influence of the materials on the *S. aureus* growth and adherence is presented in Fig. 13.

The antibacterial evaluation (Fig. 13) presented unique substrate-dependent modifications for all synthesized HAp materials, demonstrating a clear classification on the antibacterial effectiveness. Substrates I and II exhibited superior antibacterial properties, while Substrate III (Ti) had minimal activity, resulting in a considerable

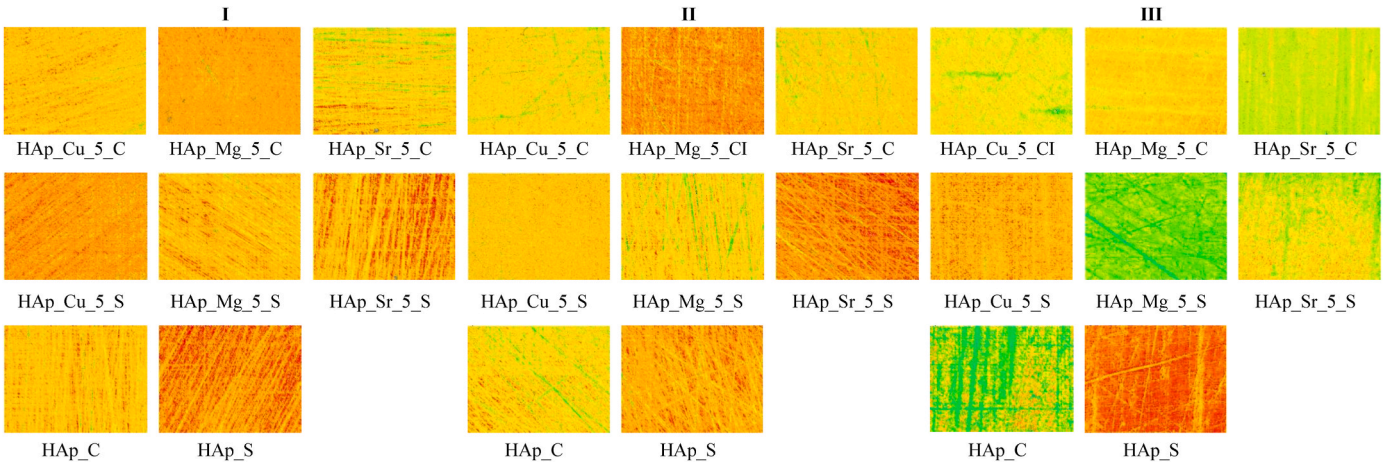

Fig. 9. Computer rendered roughness surface of deposited samples. at 40X magnification: substrates are coded as follows: substrate I – MgZnMn (Mn 0.62 Zn 4.3), substrate II - MgZnMnY (Zn 7.1 Mn 1.17 Y 1.2) and substrate III – Titanium. Cu, Mg, Sr indicate substituting ions; 5 represent concentrations (%).

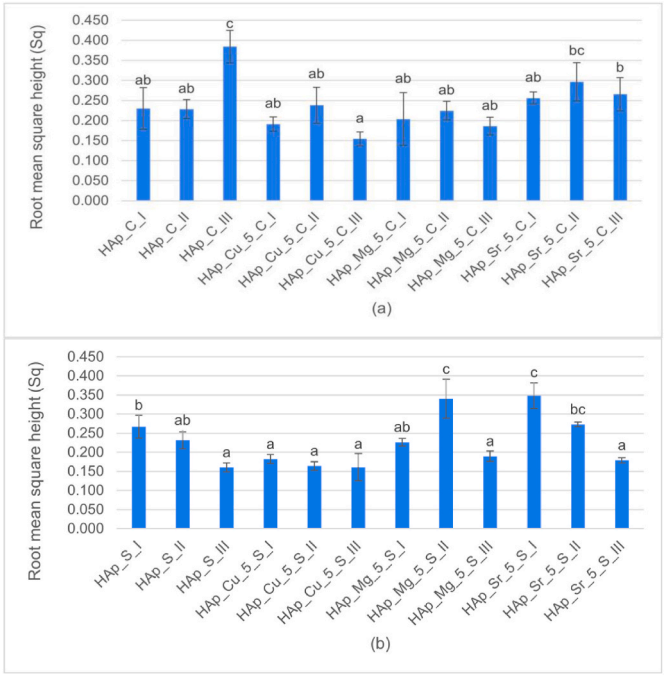

Fig. 10. Root mean square height (Sq) results of undoped and doped HAp samples: (a) synthesized by using eggshells to obtain CaO precursor and (b) synthesized by using mussel shells to obtain CaO precursor. Cu, Mg, Sr indicate substituting ions; 5 represent concentrations (%); I, II, III indicate substrates (MgZnMn, MgZnMnY, and Ti respectively). The results were calculated as mean ± SD (n = 3), different letters indicate significant differences between each sample ($p < 0.05$).

performance difference between magnesium-based and titanium substrates. In this regard, Substrate I (MgZnMn) exhibited impressive antibacterial activity, with bacterial decreases ranging from 6.2 to 8.1 logarithmic CFU/mL units, the highest antimicrobial efficacy of any studied substance. Substrate II (MgZnMnY) additionally demonstrated a suitable antibacterial effectiveness, reducing *S. aureus* biofilm development by 5.8–6.5 logarithmic CFU/mL units. Both Mg-based substrates obtained their intended superior antibacterial activity. Moreover, samples HAp_Mg_5_C_II, HAp_Sr_5_C_II, and HAp_Cu_5_S_II had strong antibacterial activity ($p < 0.001$).On the other side, Substrate III (Ti) had minimal antibacterial activity, with bacterial decreases of less than 2 logarithmic units, resulting in 85–95 % lower antimicrobial efficiency than the Mg-based substrates. This reduced efficiency of the Ti substrate emphasized once again the advantageous antibacterial properties of magnesium alloy substrates.

The conventional, unaltered implant surfaces do not have the full capacity to achieve osseointegration and preventing the growth of biofilms. Since the surface characteristics produced at the micro scale are comparable in topographical size to the colonizing microorganisms (~1 μm), they can significantly affect the formation of biofilms [86]. The growth of *Staphylococcus aureus* biofilms on the surfaces of titanium implants increases the risk of biomaterial-associated infections. Considering the type of substrates, there is a need for a unique technique that removes biofilms while also improving osseointegration of Ti implants without causing medication resistance [87]. At the same time, magnesium alloys have greater antibacterial activity than titanium. It is therefore desirable to compare various magnesium alloys based on their bacteriostatic and bactericidal properties [88].

The biocompatibility assessment (Fig. 14) revealed an opposite connection between antibacterial activity and the type of substrates. A systematic comparison of the substrates on the biological effect is also presented in Table 8. Substrate III (Ti) had the highest cell survival rate at 150–180 % compared to the control. This outstanding biocompatibility performance validates long-standing distinction of Ti as a biocompatible material and its capacity to promote the proliferation and growth of MC3T3 cell [89–92]. At the same time, Substrate I (MgZnMn) exhibits less consistent biocompatibility, with cell survival ranging from 80 to 110 % depending on the HAp formulation, resulting in a 30–50 % lower effectiveness than Substrate III. Substrate II (MgZnMnY) demonstrated a good performance, with a time-dependent biocompatibility increase from 24-h viability of 120–150 % to significantly improved 160–170 % at 48 h, indicating more substantial long-term cellular response. The addition of yttrium to the MgZnMn alloy considerably increased biocompatibility by improving surface properties while controlling ionic species release.

A comprehensive analysis of all substrates indicated that substituting ions showed specific biological effects according to the substrate. Incorporating Sr^{2+} and Mg^{2+} increased cell viability by 10–20 % in comparison with undoped samples on Substrates I and II, and 5–15 % on Substrate III, suggesting favorable effects on cellular processes and material surface modulation [93,94]. Cu^{2+} incorporation reduced cell viability by 15–25 % on Substrate I, 5–10 % on Substrate II, and less than 5 % on Substrate III, indicating that Ti could decrease Cu^{2+}-induced cytotoxicity. Furthermore, the CaO precursor source had a significant impact on biological performance, with eggshell-derived HAp coatings demonstrating 12–18 % higher cell viability across all substrates compared to mussel shell-derived samples, particularly in Substrate II

Table 5
Surface roughness parameters (valley depth, peak-to-valley height, arithmetic mean height, and root mean square height) of undoped and doped HAp samples: (a) synthesized by using eggshells to obtain CaO precursor and (b) synthesized by using mussel shells to obtain CaO precursor. Cu, Mg, Sr indicate substituting ions; 5 represent concentrations (%); I, II, III indicate substrates (MgZnMn, MgZnMnY, and Ti respectively).

(a) .

Samples	HAP_C			HAp_Cu_5_C			HAp_Mg_5_C			HAp_Sr_5_C		
Substrate	I	II	III	I	II	III	I	II	III	I	II	III
Valley depth (Sv)	1.923	1.634	1.201	2.376	2.080	1.252	2.591	2.048	1.763	1.921	1.769	2.939
Maximum peak to valley height (St)	3.570	2.880	2.807	3.697	3.553	2.473	4.425	3.222	2.972	3.350	3.252	5.174
Arithmetic mean height (Sa)	0.155	0.154	0.337	0.121	0.158	0.107	0.114	0.152	0.129	0.173	0.225	0.177
Root mean square height (Sq)	0.230	0.228	0.384	0.191	0.238	0.154	0.204	0.224	0.186	0.256	0.296	0.266

(b) .

Samples	HAp_S			HAp_Cu_5_S			HAp_Mg_5_S			HAp_Sr_5_S		
Substrate	I	II	III	I	II	III	I	II	III	I	II	III
Valley depth (Sv)	1.945	2.350	1.464	1.635	1.988	1.518	2.249	2.438	1.234	2.198	2.361	1.141
Maximum peak to valley height (St)	3.318	3.798	2.580	2.640	3.389	2.656	3.593	4.128	2.635	3.861	3.910	2.428
Arithmetic mean height (Sa)	0.204	0.162	0.111	0.113	0.098	0.115	0.153	0.204	0.125	0.282	0.177	0.130
Root mean square height (Sq)	0.267	0.232	0.160	0.182	0.164	0.161	0.226	0.340	0.190	0.348	0.273	0.179

Table 6
Overall surface roughness parameters comparison.

Dopant	Overall Roughness Level	C vs S Comparison
Undoped HAp	Medium	C-series > S-series in Sv & St (especially Groups I & II); C-series has deeper valleys and higher peaks; S-series surfaces are more uniform and smoother.
Cu	Low	Very minor differences; S-series slightly smoother overall; Cu-doping leads to smooth surfaces
Mg	Medium-Low	S-series ≈ C-series; Sa & Sq slightly higher in S-series; Mg-doping leads to moderate roughness; more consistent behavior in S-series; low overall variation.
Sr	High	S-series > C-series in all parameters (especially I & II); Sr enhances roughness and heterogeneity

C represents the samples prepared by using eggshells as CaO precursors, and S represents the samples prepared by using mussel shells as CaO precursors.

Table 7
The corrosion rate through the immersion test of I - MgZnMn alloy, II - MgZnMnY alloy, and III – Titanium.

Precursor	Dopant	Corrosion Rate(mm/year)		
		Substrate I	Substrate II	Substrate III
Eggshell (C)	Undoped	+1.095	−2.008	+0.243
	Cu (5 %)	−0.634	−0.892	+0.382
	Mg (5 %)	+0.432	−3.290	−0.185
	Sr (5 %)	−6.885	−0.084	+0.428
Mussel shells (S)	Undoped	−0.893	−0.279	+0.127
	Cu (5 %)	+1.527	+3.402	−0.093
	Mg (5 %)	+3.745	+0.613	−0.359
	Sr (5 %)	−3.399	−1.199	−0.023

HAp samples.

Based on the obtained results, samples obtained using the CaO precursor derived from eggshells showed higher cell viability than samples obtained using the CaO precursor derived from mussel shells.

In conclusion, our findings provide useful insights into the selection of appropriate substrate materials as well as the significance of various dopants in boosting the samples' biological performance. Substrate III (Ti) provides excellent biocompatibility but minimal antibacterial protection, while Substrate II (MgZnMnY) attains the ideal balance between excellent antibacterial activity and good-to-excellent biocompatibility for long-term applications. Moreover, Substrate I (MgZnMn) provides superior antimicrobial activity with moderate biocompatibility for high-risk infection applications. These findings provide useful insights for the selection and optimization of substrate materials and substituting ion selection for biomedical applications. The statistical significance was evaluated by one-way analysis of variance (ANOVA). A value of p less than 0.05 was considered significant.

4. Discussion

Bioactive coatings are commonly applied to implant surfaces to improve their integration with the osseous tissue. Among these coatings, HAp stands out as the preferred selection due to its similar chemical and structural properties of the mineral phase in bones. Due to these similarities, HAp may assist in bone healing effectively. HAp ceramics, on the other hand, are naturally fragile, making them unsuitable for heavy-duty applications. Recently, researchers have concentrated on producing HAp from biogenic materials like eggshells and seashells. These natural sources have demonstrated the potential to improve the material's ability to mimic the chemical structure of human bone, resulting in increased biocompatibility and tissue regeneration. Furthermore, HAp produced from natural sources exhibits excellent biocompatibility and antimicrobial properties, making it ideal for biomedical applications.

This work investigated the interaction between material synthesis, structural modifications, surface deposition, and biological performance using a unique approach that involves calcium sources derived from natural products, ion substitution variations, and material substrates. The XRD evaluation validated the effective synthesis of both undoped and doped HAp samples, highlighting the potential of using environmentally friendly and ecologically sourced precursors like eggshells and mussel shells.

The characteristic HAp diffraction peaks were confirmed according to literature data, strengthening the structural integrity of the synthesized samples. Additionally, this study investigated how substituting ions affected the structural characteristics and crystallinity of HAp. By identifying the corresponding functional groups, FT-IR spectroscopy provided supplementary proof of HAp synthesis to validate the successful synthesis [24,95,96]. The broadening of OH vibration bands in doped samples confirmed the interactions between substituting ions and the HAp lattice, leading to alteration of group mobility [97]. Furthermore, the decrease in OH intensity with ion substitution suggested changes in HAp lattice, consistent with the XRD findings. On the other side, the presence of HAp functional groups in all samples confirmed the chemical stability of the doped structures, essential for maintaining the bioactivity of the developed sample.

The morphological and microstructural properties of the obtained materials were also investigated. SEM analysis highlighted a slight

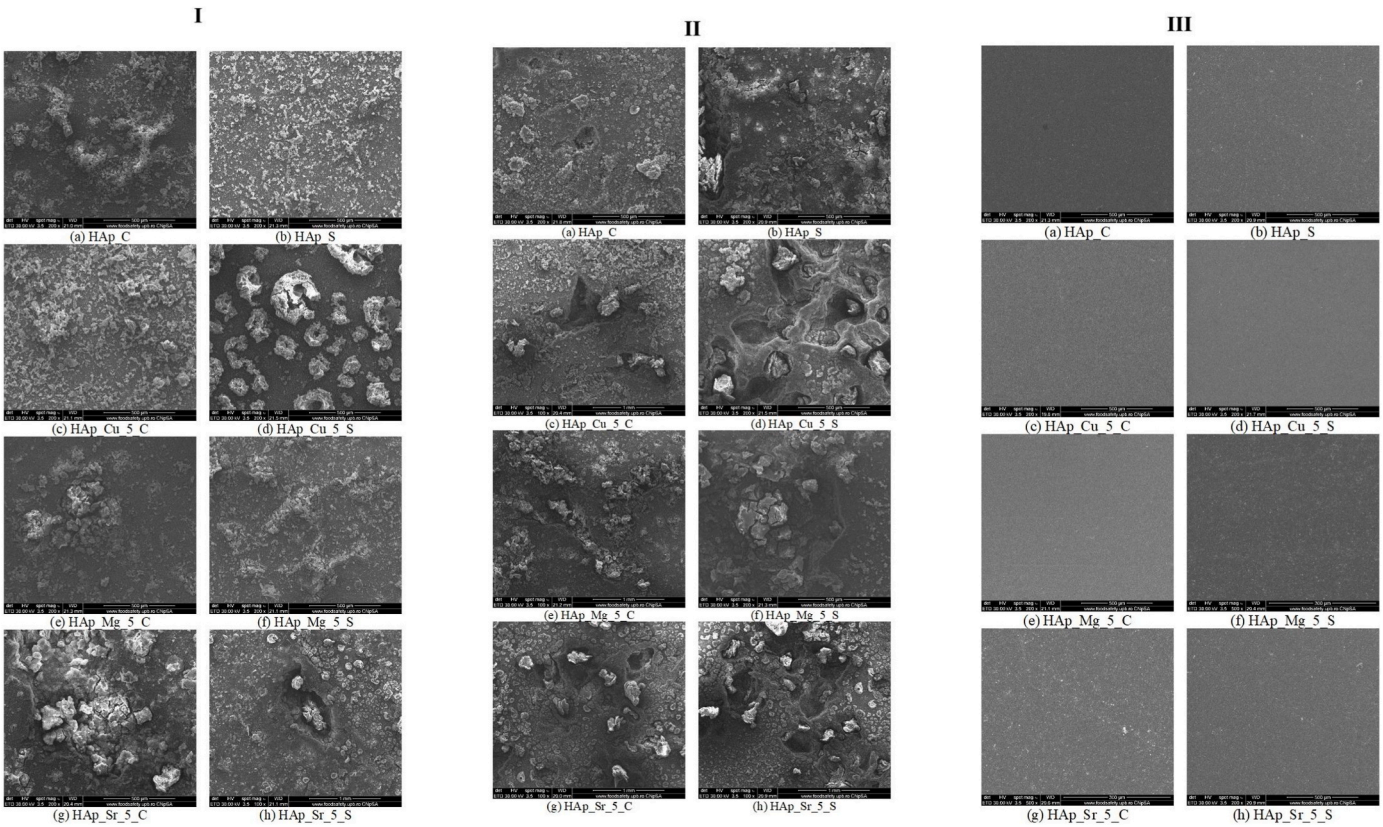

Fig. 11. SEM micrographs of the deposited coatings after being submerged in SBF solution for 168 h. Cu, Mg, Sr indicate substituting ions; 5 represent concentrations (%); I, II, III indicate substrates (MgZnMn, MgZnMnY, and Ti respectively).

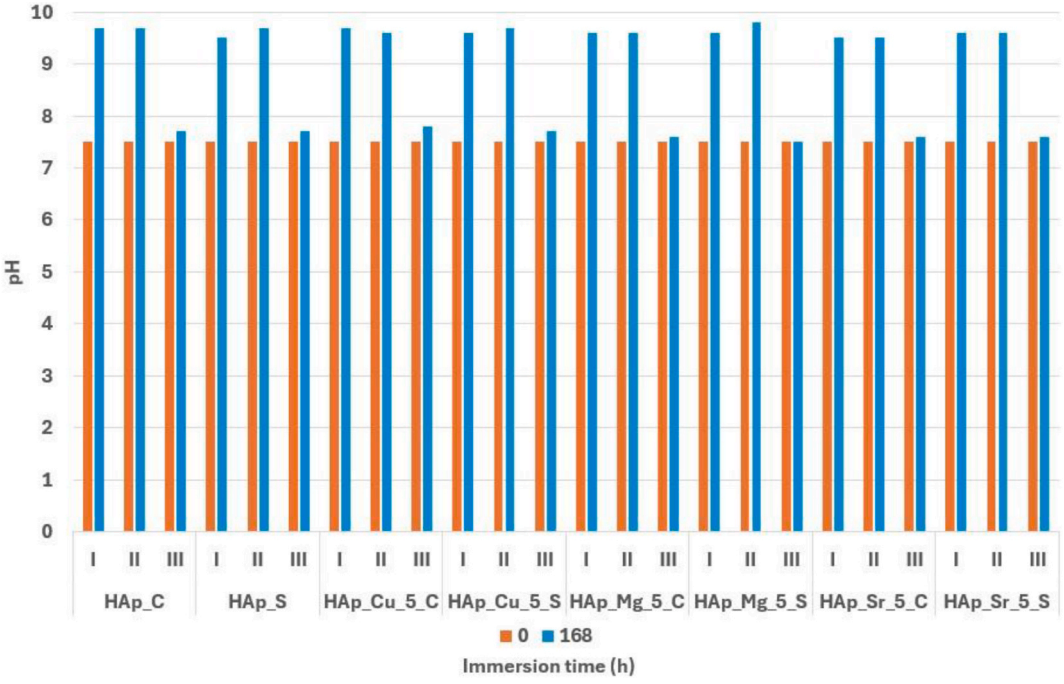

Fig. 12. pH variation of SBF at the different immersion periods. Cu, Mg, Sr indicate substituting ions; 5 represent concentrations (%); I, II, III indicate substrates (MgZnMn, MgZnMnY, and Ti respectively).

influence on the morphology of the developed samples. These changes are influenced by precursor sources and doping concentration. SEM research suggested that eggshell-derived HAp particles varied from 3 to 25 nm, whereas mussel shell-derived particles were 4–29 nm. These particle size variations reflect agglomerates of the crystallites determined through XRD. The crystallite sizes from Rietveld refinement

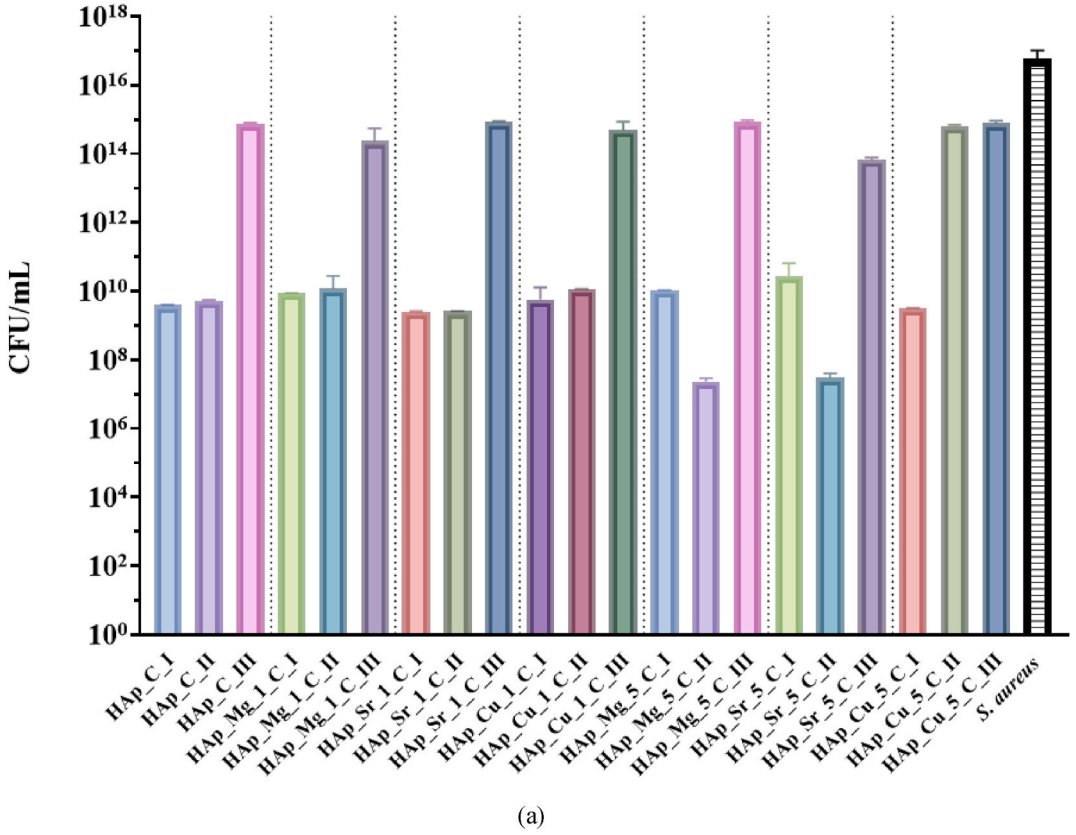

(a)

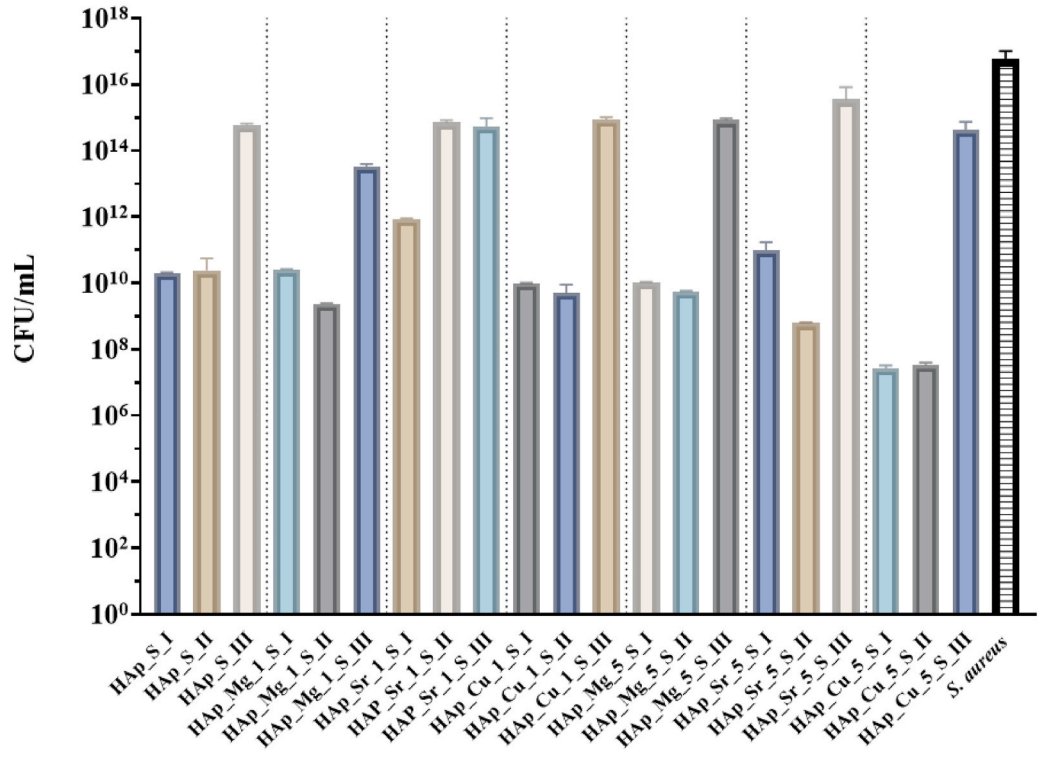

(b)

Fig. 13. The anti-adherent capacity of undoped and doped HAp samples obtained by using (a) eggshells and (b) mussel shells. The data results were considered statistically significant ($p < 0.001$). Cu, Mg, Sr indicate substituting ions; 1, 5 represent concentrations (%); I, II, III indicate substrates (MgZnMn, MgZnMnY, and Ti respectively).

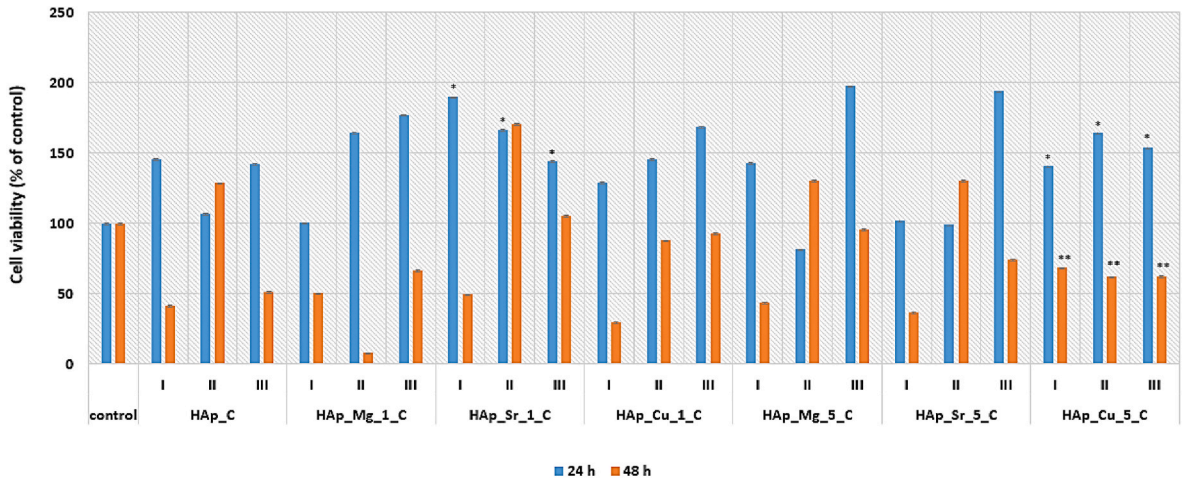

(a)

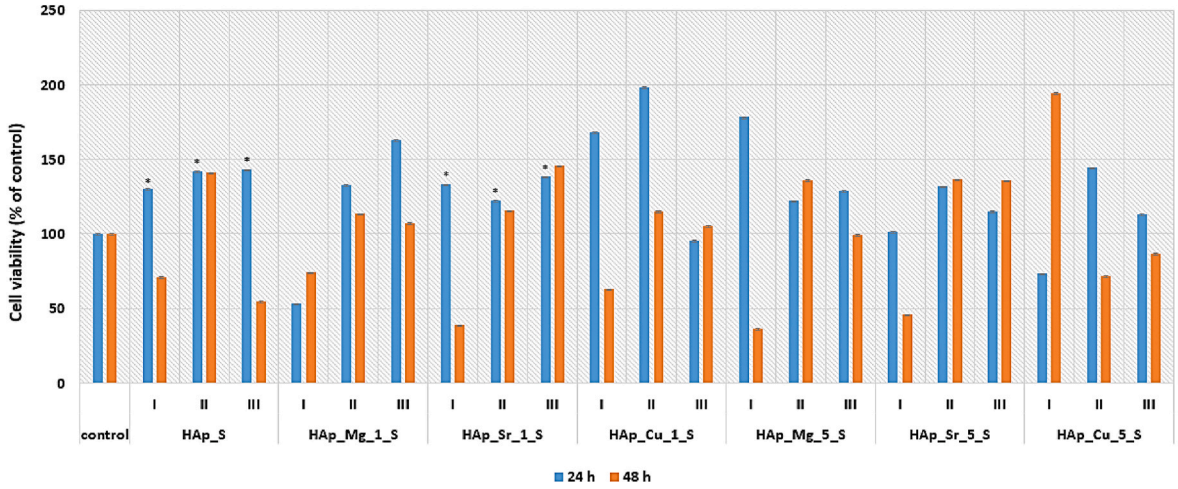

(b)

Fig. 14. Cell viability results of undoped and doped HAp samples: (a) synthesized by using eggshells to obtain CaO precursor and (b) synthesized by using mussel shells to obtain CaO precursor. The bars represent the standard deviations of the absorbances obtained, * - $p < 0.05$ and ** - $p < 0.005$. Cu, Mg, Sr indicate substituting ions; 1, 5 represent concentrations (%); I, II, III indicate substrates (MgZnMn, MgZnMnY, and Ti respectively).

Table 8
Comparison of biological activity of the developed coatings.

Substrate	Material	Coating Characteristics	Antibacterial Activity	Biocompatibility	Applicability
I	MgZnMn	High porosity, rough texture	Excellent (6–8 log reduction)	Moderate (variable viability)	High-risk infection environments (superior infection resistance)
II	MgZnMnY	Moderate porosity, uniform texture	Excellent (6 log reduction)	Good-to-excellent (120–170 % viability)	Biodegradable implants for extended use (enhanced long-term performance)
III	Titanium	Low porosity, smooth, uniform texture	Minimal activity	Excellent (>150 % viability)	Load-bearing permanent implants (osseointegration)

(Table 3) revealed that undoped eggshell-derived HAp had larger crystallites (13.6 nm) than mussel shell-derived HAp (8.1 nm), suggesting distinct crystal growth processes even though the overall particle size are similar. The modifications in unit cell parameters due to doping were consistent with ionic radius differences: Sr^{2+} doping increased unit cell volume due to its larger ionic radius, while Cu^{2+} and Mg^{2+} produced minor expansions. The crystallite size calculations revealed that both precursor source and dopant concentration influenced crystal development, while higher doping ion concentrations decreasing crystallite sizes, especially in Cu-doped materials.

Furthermore, by increasing the doping concentration, the tendency of nanoparticles to agglomerate increased and at the same time with morphological changes, suggesting that substituting ion sizes and concentrations affected particle formation mechanisms. The same analysis was performed for the coated samples. The film depositions derived from these HAp samples presented diverse surface textures and porosity based on the substrate and precursor type. Eggshell-based coatings exhibited greater porosity, which could lead to the enhancement in bioactivity and osseointegration, whereas mussel shell-based coatings provided a smoother, denser surface, potentially improving mechanical

stability. The substrate material also influenced coating uniformity. In this regard, the titanium substrates demonstrated superior smoothness and reduced abrasion, attributes beneficial for long-term implant performance.

The applicability of the obtained coating in medical device was evaluated with the aid of biological investigations of HAp-coated substrates. Quantitative surface studies demonstrate a clear mechanical connection between surface properties, corrosion behavior and biological activity. In this regard, Substrate I (MgZnMn) has the most pronounced surface characteristics, with Sq values between 0.204 and 0.267 μm and St values up to 4.425 μm, resulting in highly rough structures that affects *S. aureus* biofilm development. The rough structure creates several contact areas that physically inhibit biofilm matrix growth, resulting in a significant 6–8 logarithmic CFU/mL reduction, but it also increases penetration into the substrate, which leads to greater corrosion rates and compromises long-term coating stability. This corrosion to the surface explains the variation in biocompatibility (80–110 %) of the substrate, as extreme roughness combined with uncontrolled corrosion results in an unstable cellular environment.

Substrate II (MgZnMnY) possesses an optimal surface architecture with moderate Sq values (0.162–0.340 μm) and controlled St values (3.2–4.1 μm), resulting in outstanding antibacterial activity (6–6.5 log reduction). The time-dependent biocompatibility increases from 120 to 150 % at 24 h to 160–170 % at 48 h strongly correlates with this enhanced topography, as cells require time to migrate and attach on the moderately rough surface before they proliferate. Substrate III (Ti) has a smooth, uniform surface with low Sq values, resulting in excellent biocompatibility (>150 % cell survival). However, this smoothness leads to minimal antibacterial activity (<2 log reduction), emphasizing the importance of balancing surface roughness and biological function. To sustain this, Hernández [93] also mentioned that Mg alloys present the capacity to control the corrosion rate. Moreover, Liang et al. [98] supported that the incorporation of yttrium (Y) to the metal has the possibility to improve its strength and ductility. Furthermore, its addition in magnesium alloys did not highlight any significant toxicity to osteoblasts. Doping ions also presented a significant influence on biological performance. Furko et al. [99] mentioned that Sr^{2+} is well-known for its dual benefit in the promotion of bone formation and decrease of bone resorption. This incorporating ion has the capacity to enhance pre-osteoblastic cell replication and stimulate new bone formation through osteogenesis and differentiation into osteoblasts, while inhibiting the activity of osteoclasts. At the same time, Mg^{2+} doping enhances osteoblast adhesion strength. While Mg^{2+} and Sr^{2+} enhanced cell viability, due to their beneficial effects on cellular processes and material surface modulation, Cu^{2+} incorporation demonstrated cytotoxic effects at higher concentrations, emphasizing the necessity to optimize the dopant concentration to balance antimicrobial properties with biocompatibility. As previously mentioned, the study demonstrated a dose-dependent cytotoxicity with Cu^{2+} uptake, that corresponds to the well-know mechanisms of Cu-induced cellular toxicity [100]. Cu toxicity is primarily triggered by its role in the formation of reactive oxygen species (ROS), which modifies the structure and function of essential biomolecules. Cu^{2+}-induced cytotoxicity occurs when Cu levels surpass cellular requirements or are improperly distributed within cells [101,102]. Li et al. [103] reported that the half maximal inhibitory concentration (IC50) for Cu^{2+} varies by cell type, with values around 134.6 μM for MC3T3-E1 osteoblastic cells. The concentrations less than 10–222 μM have been reported shown to be safe and beneficial for cell proliferation. The toxicity of Cu-containing nanoparticles often differs from bulk materials due to their high surface area-to-volume ratio and unique surface chemistry properties, which influence ion release kinetics and cellular interactions [100,104]. The reduced cell viability observed with higher Cu^{2+} concentrations (5 %) compared to lower concentrations (1 %) in our HAp coatings demonstrates the critical importance of optimizing dopant levels to balance antimicrobial efficacy with biocompatibility. Future studies should include comprehensive dose-response analyses with IC50 determinations to establish precise safety margins for Cu-doped HAp formulations in biomedical applications, particularly considering the substrate-dependent variations in ion release and cellular response observed in our work. Due to their high surface area-to-volume ratio and unique surface chemistry features, Cu-containing nanoparticles have a different toxicity than bulk materials [102]. The optimization of dopant concentrations is essential for optimizing antibacterial activity and biocompatibility, as seen by reduced cell viability for the samples containing Cu^{2+} with the highest concentrations. Future research needs to incorporate comprehensive dose-response analyses with IC50 determinations to determine precise limits of safety for Cu-doped HAp formulations in biomedical applications.

The source of the precursor also had an impact on surface properties and biological performance. Eggshell-derived HAp exhibited larger crystallites in comparison with mussel shell-derived HAp, with increased surface porosity, leading to improved biocompatibility (12–18 % greater cell survival).This improvement corresponds with the increased surface roughness reported in profilometry studies (Table 5), where eggshell-derived samples exhibited higher Sq values. Mussel shell-derived HAp resulted in denser, uniform coatings with controlled surface roughness, providing superior mechanical stability while maintaining suitable biological activity. The biocompatibility of eggshell-derived HAp might result from the integration of surface porosity and appropriate roughness characteristics that promote cell adhesion and proliferation. The correlation between crystallite size and biological activity is significant. While smaller crystallites provide larger surface areas, the observed biological effects may be affected by several factors, such as surface roughness (as demonstrated by profilometry data), coating porosity (observed in SEM), and the particular substrate material, rather than solely crystallite size.

The study demonstrates that appropriate biomedical efficiency requires a suitable balance of surface structure, corrosion resistance, and biological compatibility. Several samples showed negative corrosion rates, indicating active biomineralization processes with moderate surface roughness (Sa ~0.2–0.4 μm) and increased biological activity. The Sr-doped HAp on MgZnMnY substrate provides an optimal balance of surface roughness (Sq ~0.273 μm) that facilitates cell adhesion and corrosion-induced biomineralization (−1.199 mm/year), resulting in good biocompatibility (160–170 % cell survival). This substrate-coating system demonstrates how surface engineering might optimize numerous performance parameters.

The purpose of this work was to optimize the synthesis and utilization of HAp materials in tissue engineering. To achieve this purpose, the research focused on selecting a natural source for the CaO precursor, identifying the optimal replacing ion, and integrating the substrate. Furthermore, the use of sustainable CaO sources such as eggshells offers a feasible approach for long-term material development in biomedical applications.

5. Conclusions

This study presents a unique proposal for generating bioactive implant coatings by using CaP precursors obtained from natural sources. Our comprehensive research shows that these biogenic sources efficiently create outstanding HAp coatings via MAPLE deposition, making them a feasible alternative to standard synthetic precursors.

Systematic analysis using XRD and FTIR spectroscopy confirmed the effective synthesis of both pure and ion-doped HAp, confirming the structural integrity and phase purity of the material. Doping ions (Mg^{2+}, Sr^{2+}, Cu^{2+}) were included to control coating properties. Each dopant offered specific features that influenced the structure of the material and biological performance.

In this regard, our findings show that substrate selection has a significant impact on final coating performance. The study showed major distinctions in performance between substrate types, with some

excelling in biocompatibility and others demonstrating higher antibacterial efficiency. This substrate-dependent activity offers useful insights for adjusting coatings to specific therapeutic needs.

Moreover, the optimization of dopant concentrations is a significant aspect in obtaining the balance of antibacterial activities and biocompatibility. While certain dopants improved cellular responses and promoted biological activity, others needed precise concentration control to avoid adverse effects. This insight permits the development of formulations particular to the application coating.

This study effectively addresses the connection between sustainable material synthesis and enhanced biomedical applications by demonstrating that waste-derived Ca sources may generate clinically useful biomaterials. The study offers the foundation for environmentally friendly biomaterial development while addressing both challenges of promoting osseointegration and minimizing bacterial colonization in orthopedic implants.

CRediT authorship contribution statement

Diana-Elena Radulescu: Conceptualization, Formal analysis, Investigation, Methodology, Visualization, Writing – original draft, Writing – review & editing. **Bogdan Stefan Vasile:** Conceptualization, Data curation, Investigation, Methodology, Project administration, Resources, Funding acquisition, Supervision, Formal analysis, Writing – original draft, Writing – review & editing. **Vasile-Adrian Surdu:** Data curation, Formal analysis, Methodology, Software, Writing – original draft. **Roxana Doina Trusca:** Data curation, Formal analysis, Software. **Alexandra Catalina Birca:** Data curation, Formal analysis, Investigation, Software, Methodology. **Cornelia-Ioana Ilie:** Data curation, Formal analysis, Software, Writing – original draft. **Lia-Mara Ditu:** Data curation, Formal analysis, Software. **Ludmila Motelica:** Formal analysis, Software, Validation. **Ionela Andreea Neacsu:** Conceptualization, Investigation, Methodology, Project administration, Supervision, Validation, Visualization, Writing – original draft, Writing – review & editing. **Iulian Boerasu:** Data curation, Formal analysis, Methodology, Software, Writing – original draft. **Simona Brajnicov:** Data curation, Formal analysis, Methodology, Software, Writing – original draft. **Cosmin Iulian Codrea:** Software, Investigation, Methodology, Writing – review & editing. **Ecaterina Andronescu:** Conceptualization, Investigation, Methodology, Project administration, Supervision, Validation, Visualization, Writing – original draft, Writing – review & editing.

Declaration of competing interest

The authors declare that they have no known competing financial interests or personal relationships that could have appeared to influence the work reported in this paper.

Acknowledgements

This work was supported by the Romanian Government through the National Program “Installations and Strategic Objectives of National Interest” for access to research infrastructure National Research Center for Micro and Nanomaterials from the National University of Science and Technology Politehnica Bucharest.

References

[1] Das A, Saxena V, Bhardwaj A, Rabha S, Pandey LM, Dobbidi P. Microstructural, interfacial, biological and electrical activity in sputtered hydroxyapatite-barium strontium titanate bilayered thin films. Surf Interfaces 2022;31:102063.
[2] Islas-García E, Torres- SanMiguel CR, Trejo-Valdez M, Mercado-Zúñiga C, Ramírez-Crescencio F, Villarroel R, Torres-Torres C, García-Merino JA. Interferometric characterization of high-frequency piezoelectric effects in hydroxyapatite thin films. Sensor Actuator Phys 2024;372:115327.
[3] Predoi D, Ţălu Ş, Carmen Ciobanu S, Iconaru SL, Saraiva Matos R, Duarte da Fonseca Filho H. Exploring the physicochemical traits, antifungal capabilities, and 3D spatial complexity of hydroxyapatite with Ag+Mg2+ substitution in the biocomposite thin films. Micron 2024;184:103661.
[4] Oladijo SS, Akinlabi ET, Jen TC, Mwema FM, Oladijo OP. Effect of power and deposition time on sputtered hydroxyapatite thin film coatings on stainless steel 304. Mater Today Proc 2022;62:4584–8.
[5] Hassan MK, Abdelrehim SAA, Elkhooly TA, Elmezayyen AS, Mansour-Gabr MM, Abdel Ghany NA. Investigation of structure, morphology, and corrosion behavior of carboxylic acids/hydroxyapatite/chitosan coatings on Ti discs for implants. Thin Solid Films 2024;798:140378.
[6] Veluswamy R, Balasubramaniam G, Natarajan M, Krishnaswamy M, Chinnappan BA, Nagarajan S, Subramanian B, Velauthapillai D. Multifunctional and sustainable hydroxyapatite from natural products for biomedical and industrial applications - a comprehensive review. Sustain Chem Pharm 2024;41:101653.
[7] Sudhakar MP, Ali S, Chitra S. Scrutinizing the effect of rGO-cuttlefish bone hydroxyapatite composite infused carrageenan membrane towards wound reconstruction. Int J Biol Macromol 2024;262:130155.
[8] Wibisono Y, Pratiwi AY, Octaviani CA, Fadilla CR, Noviyanto A, Taufik E, Uddin MKH, Anugroho F, Rochman NT. Marine-derived biowaste conversion into bioceramic membrane materials: contrasting of hydroxyapatite synthesis methods. Molecules 2021;26:6344.
[9] Fathyunes L, Hosseini M, Khalil-Allafi J. In-vitro biocompatibility, antibacterial activity, and corrosion resistance of HA-TiO2/ZnO coating fabricated by plasma electrolytic oxidation on Ti6Al4V. Mater Today Commun 2024;40:109443.
[10] Cristina Rodica Dumitrescu IAN, Surdu Vasile Adrian, Nicoara Adrian Ionut, Codrea Cosmin Iulian, Emilian Pop Cristian, Trusca Roxana, Andronescu Ecaterina. Maturation of hydroxyapatite from biogenic calcium source – a comparative study. UPB Sci Bull 2022;84:12.
[11] Karunakaran G, Cho E-B, Kumar GS, Kolesnikov E, Janarthanan G, Pillai MM, Rajendran S, Boobalan S, Sudha KG, Rajeshkumar MP. Mesoporous Mg-doped hydroxyapatite nanorods prepared from bio-waste blue mussel shells for implant applications. Ceram Int 2020;46:28514–27.
[12] Goh KW, Wong YH, Ramesh S, Chandran H, Krishnasamy S, Ramesh S, Sidhu A, Teng WD. Effect of pH on the properties of eggshell-derived hydroxyapatite bioceramic synthesized by wet chemical method assisted by microwave irradiation. Ceram Int 2021;47:8879–87.
[13] Habib ML, Disha SA, Sahadat Hossain M, Uddin MN, Ahmed S. Enhancement of antimicrobial properties by metals doping in nano-crystalline hydroxyapatite for efficient biomedical applications. Heliyon 2024;10:e23845.
[14] Uysal I, Yilmaz B, Evis Z. Zn-doped hydroxyapatite in biomedical applications. Journal of the Australian Ceramic Society 2021;57:869–97.
[15] Panda S, Biswas CK, Paul S. A comprehensive review on the preparation and application of calcium hydroxyapatite: a special focus on atomic doping methods for bone tissue engineering. Ceram Int 2021;47:28122–44.
[16] Li X, Lin E, Wang K, Ke R, Kure-Chu S-Z, Xiao X. Fabrication and characterization of hydroxyapatite coatings on anodized magnesium alloys by electrochemical and chemical methods intended for biodegradable implants. Ceram Int 2024;50:36838–48.
[17] Asemabadi Z, Amir Naderi A, Zolfigol F, Mokhtari J, Eivaz Mohammadloo H. Comparative investigation of EDTA and zein polymer presence on hydroxyapatite coating for Mg-based implant application: electrochemical, microstructure and anti-bacterial properties. Mater Res Bull 2024;174:112735.
[18] Wang T, Yang G, Zhou W, Hu J, Jia W, Lu W. One-pot hydrothermal synthesis, in vitro biodegradation and biocompatibility of Sr-doped nanorod/nanowire hydroxyapatite coatings on ZK60 magnesium alloy. J Alloys Compd 2019;799:71–82.
[19] Codrea CI, Lincu D, Atkinson I, Culita DC, Croitoru A-M, Dolete G, Trusca R, Vasile BS, Stan MS, Ficai D, Ficai A. Comparison between two different synthesis methods of strontium-doped hydroxyapatite designed for osteoporotic bone restoration. Materials 2024;17:1472.
[20] Sasireka A, Renji R, Mohan Raj R, Vignesh S, Raj V, Ashraf IM, Shkir M. Exploration on in vitro bioactivity, antibacterial activity and corrosion behavior of strontium doped hydroxyapatite reinforced chitosan-polypyrrole/TNT for bone regeneration. Inorg Chem Commun 2022;142:109621.
[21] Matić T, Zebić ML, Miletić V, Cvijović-Alagić I, Petrović R, Janaćković D, Veljović D. Sr,Mg co-doping of calcium hydroxyapatite: hydrothermal synthesis, processing, characterization and possible application as dentin substitutes. Ceram Int 2022;48:11155–65.
[22] Radulescu D-E, Vasile OR, Andronescu E, Ficai A. Latest research of doped hydroxyapatite for bone tissue engineering. Int J Mol Sci 2023;24:13157.
[23] Ressler A, Žužić A, Ivanišević I, Kamboj N, Ivanković H. Ionic substituted hydroxyapatite for bone regeneration applications: a review. Open Ceramics 2021;6:100122.
[24] Unabia RB, Bonebeau S, Candidato RT, Jouin J, Noguera O, Pawłowski L. Investigation on the structural and microstructural properties of copper-doped hydroxyapatite coatings deposited using solution precursor plasma spraying. J Eur Ceram Soc 2019;39:4255–63.
[25] Fadli A, Prabowo A, Reni Yenti S, Huda F, Annisa Liswani A, Lamsinar Br Hutauruk D. High performance of coating hydroxyapatite layer on 316L stainless steel using ultrasonically and alkaline pretreatment. J King Saud Univ Sci 2023;35:102681.
[26] Akazawa H. Characterization of crystallographic orientation and lattice disorder in hydroxyapatite thin films by raman scattering. Ceram Int 2022;48:624–31.
[27] Liao J, Li X, Xuan S, Zhang W, Li G, Li H. Modulating the corrosion performance of magnesium alloys through hydroxyapatite coating. Chem Eng J 2024;495:153550.

[28] Dragomir L, Antoniac A, Manescu V, Robu A, Dinu M, Pana I, Cotrut CM, Kamel E, Antoniac I, Rau JV, Vladescu A. Preparation and characterization of hydroxyapatite coating by magnetron sputtering on mg–zn–ag alloys for orthopaedic trauma implants. Ceram Int 2023;49:26274–88.
[29] Mozetič M. Surface modification to improve properties of materials. Materials 2019;12:441.
[30] Hosseini M, Khalil-Allafi J, Etminanfar M, Safavi MS, Bloise N, Ghalandarzadeh A. Tackling the challenges facing the clinical applications of pure PEO hydroxyapatite layers: co-deposition of YSZ nanoparticles. Mater Chem Phys 2023;293:126899.
[31] Huang Y, Qiao H, Nian X, Zhang X, Zhang X, Song G, Xu Z, Zhang H, Han S. Improving the bioactivity and corrosion resistance properties of electrodeposited hydroxyapatite coating by dual doping of bivalent strontium and manganese ion. Surf Coating Technol 2016;291:205–15.
[32] Safari-Gezaz M, Parhizkar M, Asghari E. Investigation of the structural properties of Si4+-doped HAP coatings on Ti-6Al-4V substrate as a corrosion barrier in biomedical media. Colloids Surf A Physicochem Eng Asp 2024;699:134742.
[33] Rajkumar P, Sarma BK. Substrate dependent structural variations of biomimetic carbonated hydroxyapatite deposited on glass, Ti and sputtered ZnO thin films. Mater Char 2022;191:112120.
[34] Acar MT, Kovacı H, Çelik A. Improving the wettability and corrosion behavior of Cp-Ti by applying anodization surface treatment with the addition of boric acid, graphene oxide and hydroxyapatite. Mater Today Commun 2022;31:103683.
[35] Safavi MS, Khalil-Allafi J, Motallebzadeh A, Volpini C, Khalili V, Visai L. Encouraging tribomechanical and biological responses of hydroxyapatite coatings reinforced by various levels of niobium pentoxide particles. Mater Adv 2023;4:5618–32.
[36] Su Y, Li K, Tielens F, Wang J. Effect of sprayed techniques on the surface microstructure and in vitro behavior of nano-HAp coatings. Mater Sci Eng C 2020;117:111318.
[37] Yashiro H, Takashima H, Ohmura H, Kakehata M, Kawagoe D. Optical properties of β-tricalcium phosphate and hydroxyapatite for droplet-free hydroxyapatite coating by pulsed-laser deposition. Vacuum 2025;239:114331.
[38] Sun J, Jing X, Zheng S, Shi B, Imran Jaffery SH, Zhang D. Fabrication of porous surface by liquid-assisted laser ablation for enhancing hydroxyapatite deposition in zirconia. Ceram Int 2025;51:12963–75.
[39] Dinu M, Ivanova AA, Surmeneva MA, Braic M, Tyurin AI, Braic V, Surmenev RA, Vladescu A. Tribological behaviour of RF-magnetron sputter deposited hydroxyapatite coatings in physiological solution. Ceram Int 2017;43:6858–67.
[40] Kumar R, Shikha D, Sinha SK. Improvement in bioactivity, hardness and friction resistance of 3 % manganese-doped hydroxyapatite coated on alumina using radio frequency magnetron sputtering. Surf Coating Technol 2024;494:131481.
[41] Russo T, Peluso V, Gloria A, Gargiulo V, Alfe M, Ausanio G. An integrated design strategy coupling additive manufacturing and matrix-assisted pulsed laser evaporation (MAPLE) towards the development of a new concept 3D scaffold with improved properties for tissue regeneration. Nanoscale Adv 2024;6:3064–72.
[42] Rusen E, Brîncoveanu O, Dincă V, Toader G, Diacon A, Dinescu MA, Mocanu A. Surface pre-treatment of aluminum alloy for mechanical improvement of adhesive bonding by maple-assisted pulsed laser evaporation technique. RSC Adv 2024;14:22627–41.
[43] Chen J, Liu J, Deng H, Yao S, Wang Y. Regulatory synthesis and characterization of hydroxyapatite nanocrystals by a microwave-assisted hydrothermal method. Ceram Int 2020;46:2185–93.
[44] Burdusel A-C, Neacsu IA, Birca AC, Chircov C, Grumezescu A-M, Holban AM, Curutiu C, Ditu LM, Stan M, Andronescu E. Microwave-assisted hydrothermal treatment of multifunctional substituted hydroxyapatite with prospective applications in bone regeneration. J Funct Biomater 2023;14:378.
[45] Nicoara AI, Stoica AE, Ene D-I, Vasile BS, Holban AM, Neacsu IA. In situ and Ex situ designed hydroxyapatite: bacterial cellulose materials with biomedical applications. Materials 2020;13:4793.
[46] Neacsu IA, Arsenie LV, Trusca R, Ardelean IL, Mihailescu N, Mihailescu IN, Ristoscu C, Bleotu C, Ficai A, Andronescu E. Biomimetic Collagen/Zn2+-Substituted calcium phosphate composite coatings on titanium substrates as prospective bioactive layer for implants: a comparative study spin coating vs. MAPLE. Nanomaterials 2019;9:692.
[47] Tite T, Popa A-C, Balescu LM, Bogdan IM, Pasuk I, Ferreira JMF, Stan GE. Cationic substitutions in hydroxyapatite: current status of the derived biofunctional effects and their in vitro interrogation methods. Materials 2018;11:2081.
[48] Liu C, Chen X, Chen J, Atrens A, Pan F. The effects of Ca and Mn on the microstructure, texture and mechanical properties of Mg-4 Zn alloy. J Magnesium Alloys 2021;9:1084–97.
[49] Sun J, Zhang X, Shi Z-Z, Gao X-X, Li H-Y, Zhao F-Y, Wang J-Q, Wang L-N. Development of a high-strength Zn-Mn-Mg alloy for ligament reconstruction fixation. Acta Biomater 2021;119:485–98.
[50] Jiang MG, Xu C, Nakata T, Yan H, Chen RS, Kamado S. Development of dilute Mg–Zn–Ca–Mn alloy with high performance via extrusion. J Alloys Compd 2016;668:13–21.
[51] Tahreen N, Zhang DF, Pan FS, Jiang XQ, Li C, Li DY, Chen DL. Characterization of hot deformation behavior of an extruded Mg–Zn–Mn–Y alloy containing LPSO phase. J Alloys Compd 2015;644:814–23.
[52] Li J-a, Chen L, Zhang X-q, Guan S-k. Enhancing biocompatibility and corrosion resistance of biodegradable Mg-Zn-Y-Nd alloy by preparing PDA/HA coating for potential application of cardiovascular biomaterials. Mater Sci Eng C 2020;109:110607.
[53] Sheng LY, Du BN, Hu ZY, Qiao YX, Xiao ZP, Wang BJ, Xu DK, Zheng YF, Xi TF. Effects of annealing treatment on microstructure and tensile behavior of the Mg-Zn-Y-Nd alloy. J Magnesium Alloys 2020;8:601–13.
[54] Jaafar A, Hecker C, Árki P, Joseph Y. Sol-gel derived hydroxyapatite coatings for titanium implants: a review. Bioengineering 2020;7:127.
[55] Hieda J, Sakaguchi A, Nakano M, Akasaka H, Ohtake N. Relationships between surface energy and charge of surface-modified titanium and HAp formation. Appl Surf Sci 2019;465:509–16.
[56] Kokubo T, Kushitani H, Sakka S, Kitsugi T, Yamamuro T. Solutions able to reproduce in vivo surface-structure changes in bioactive glass-ceramic A-W3. J Biomed Mater Res 1990;24:721–34.
[57] Lemnaru Popa GM, Motelica L, Trusca RD, Ilie CI, Croitoru AM, Ficai D, Oprea O, Stoica-Guzun A, Ficai A, Ditu LM, Tihăuan BM. Antimicrobial wound dressings based on bacterial cellulose and independently loaded with nutmeg and fir needle essential oils. Polymers 2023;15.
[58] Spoială A, Ilie C-I, Dolete G, Croitoru A-M, Surdu V-A, Truşcă R-D, Motelica L, Oprea O-C, Ficai D, Ficai A, Andronescu E, Dițu L-M. Preparation and characterization of Chitosan/TiO2 composite membranes as adsorbent materials for water purification. Membranes 2022;12:804.
[59] Lemnaru Popa GM, Truşcă RD, Ilie CI, Țiplea RE, Ficai D, Oprea O, Stoica-Guzun A, Ficai A, Dițu LM. Antibacterial activity of bacterial cellulose loaded with bacitracin and amoxicillin: in vitro studies. Molecules 2020;25.
[60] CLSI, performance standards for antimicrobial susceptibility TestingCLSI supplement M100. In: Clinical and laboratory standards institute, berwyn, PA, USA; 2021.
[61] Obada DO, Salami KA, Oyedeji AN, Fasanya OO, Suleiman MU, Ibisola BA, Atta AY, Dodoo-Arhin D, Kuburi LS, Dauda M, Dauda ET. Solution combustion synthesis of strontium-doped hydroxyapatite: effect of sintering and low compaction pressure on the mechanical properties and physiological stability. Mater Lett 2021;304:130613.
[62] Sprio S, Dapporto M, Preti L, Mazzoni E, Iaquinta MR, Martini F, Tognon M, Pugno NM, Restivo E, Visai L, Tampieri A. Enhancement of the biological and mechanical performances of sintered hydroxyapatite by multiple ions doping. Frontiers in Materials 2020;7.
[63] Poovendran K, Wilson KSJ, Revathy MS, Ayeshamariam A, Kaviyarasu K. Functionalization effect of HAp with copper (Cu) having excellent dielectric applications. Surf Interfaces 2020;19:100474.
[64] Lee S-W, Balázsi C, Balázsi K, Seo D-h, Kim HS, Kim C-H, Kim S-G. Comparative study of hydroxyapatite prepared from seashells and eggshells as a bone graft material. Tissue Engineering and Regenerative Medicine 2014;11:113–20.
[65] Noori A, Hoseinpour M, Kolivand S, Lotfibakhshaiesh N, Ebrahimi-Barough S, Ai J, Azami M. Exploring the various effects of Cu doping in hydroxyapatite nanoparticle. Sci Rep 2024;14:3421.
[66] Mohammadi M, Rabiee SM, Hesaraki S. The release behavior, biocompatibility and physical properties of Ald-loaded strontium doped calcium phosphate cement. JBE 2020;17:1209–23.
[67] Baldassarre F, Altomare A, Mesto E, Lacalamita M, Dida B, Mele A, Bauer EM, Puzone M, Tempesta E, Capelli D, Siliqi D, Capitelli F. Structural characterization of low-sr-doped hydroxyapatite obtained by solid-state synthesis. Crystals 2023;13:117.
[68] Alanis-Gómez RP, Hernández-Rosas F, Olivares-Hernández JD, Rivera-Muñoz EM, Zapatero-Gutiérrez A, Méndez-Lozano N, Alanis-Gómez JR, Velázquez-Castillo R. Magnesium-doped hydroxyapatite nanofibers for medicine applications: characterization, antimicrobial activity, and cytotoxicity study. Int J Mol Sci 2024;25:12418.
[69] Li K, Li S, Ai F, Yan J, Zhou K. Fabrication and characterization of Sr-doped hydroxyapatite porous scaffold. JOM 2021;73:1745–53.
[70] Joshi KJ, Shastri NM, Shah NM. Synthesis and characterization of pure and strontium doped hydroxyapatite by sono-chemical assisted hydrothermal technique. AIP Conf Proc 2020;2220.
[71] Noviyanti AR, Rahayu I, Fauzia RP. Risdiana, the effect of Mg concentration to mechanical strength of hydroxyapatite derived from eggshell. Arab J Chem 2021;14:103032.
[72] Bystrov VS, Paramonova EV, Avakyan LA, Eremina NV, Makarova SV, Bulina NV. Effect of magnesium substitution on structural features and properties of hydroxyapatite. Materials 2023;16:5945.
[73] Unabia RB, Bonebeau S, Candidato RT, Pawłowski L. Preliminary study on copper-doped hydroxyapatite coatings obtained using solution precursor plasma spray process. Surf Coating Technol 2018;353:370–7.
[74] Othmani M, Bachoua H, Ghandour Y, Aissa A, Debbabi M. Synthesis, characterization and catalytic properties of copper-substituted hydroxyapatite nanocrystals. Mater Res Bull 2018;97:560–6.
[75] Wang B, Li Y, Wang S, Jia F, Bian A, Wang K, Xie L, Yan K, Qiao H, Lin H, Lan J, Huang Y. Electrodeposited dopamine/strontium-doped hydroxyapatite composite coating on pure zinc for anti-corrosion, antimicrobial and osteogenesis. Mater Sci Eng C 2021;129:112387.
[76] Benali Y, Predoi D, Rokosz K, Ciobanu CS, Iconaru SL, Raaen S, Negrila CC, Cimpeanu C, Trusca R, Ghegoiu L, Bleotu C, Marinas IC, Stan M, Boughzala K. Physico-chemical properties of copper-doped hydroxyapatite coatings obtained by vacuum deposition technique. Materials 2024;17:3681.
[77] Paduraru AV, Musuc AM, Oprea OC, Trusca R, Iordache F, Vasile BS, Andronescu E. Synthesis and characterization of photoluminescent Ce(III) and Ce (IV) substituted hydroxyapatite nanomaterials by Co-Precipitation method: cytotoxicity and biocompatibility evaluation. Nanomaterials 2021;11:1911.
[78] Paduraru AV, Oprea O, Musuc AM, Vasile BS, Iordache F, Andronescu E. Influence of terbium ions and their concentration on the photoluminescence

properties of hydroxyapatite for biomedical applications. Nanomaterials 2021;11:2442.
[79] Sroka-Bartnicka A, Borkowski L, Ginalska G, Ślósarczyk A, Kazarian SG. Structural transformation of synthetic hydroxyapatite under simulated in vivo conditions studied with ATR-FTIR spectroscopic imaging. Spectrochim Acta Mol Biomol Spectrosc 2017;171:155–61.
[80] Gieroba B, Przekora A, Kalisz G, Kazimierczak P, Song CL, Wojcik M, Ginalska G, Kazarian SG, Sroka-Bartnicka A. Collagen maturity and mineralization in mesenchymal stem cells cultured on the hydroxyapatite-based bone scaffold analyzed by ATR-FTIR spectroscopic imaging. Mater Sci Eng C 2021;119:111634.
[81] Ferraris S, Yamaguchi S, Barbani N, Cazzola M, Cristallini C, Miola M, Vernè E, Spriano S. Bioactive materials: in vitro investigation of different mechanisms of hydroxyapatite precipitation. Acta Biomater 2020;102:468–80.
[82] Hernández-Cortés AA, Escobedo-Bocardo JC, Cortés-Hernández DA. Influence of the alloying elements on the corrosion behavior of As-Cast magnesium–gallium–zinc alloys in simulated body fluid. Metals 2023;13:743.
[83] Li X, Sun L, Zhang P, Wang Y. Novel approaches to combat medical device-associated BioFilms. Coatings 2021;11:294.
[84] Di Domenico EG, Oliva A, Guembe M. The current knowledge on the pathogenesis of tissue and medical device-related biofilm infections. Microorganisms 2022;10:1259.
[85] Lin J, Nguyen N-YT, Zhang C, Ha A, Liu HH. Antimicrobial properties of MgO nanostructures on magnesium substrates. ACS Omega 2020;5:24613–27.
[86] Kligman S, Ren Z, Chung C-H, Perillo MA, Chang Y-C, Koo H, Zheng Z, Li C. The impact of dental implant surface modifications on osseointegration and biofilm formation. J Clin Med 2021;10:1641.
[87] Yu Y-L, Wu J-J, Lin C-C, Qin X, Tay FR, Miao L, Tao B-L, Jiao Y. Elimination of methicillin-resistant Staphylococcus aureus biofilms on titanium implants via photothermally-triggered nitric oxide and immunotherapy for enhanced osseointegration. Military Medical Research 2023;10:21.
[88] Rahim MI, Rohde M, Rais B, Seitz J-M, Mueller PP. Susceptibility of metallic magnesium implants to bacterial biofilm infections. J Biomed Mater Res 2016;104:1489–99.
[89] Vladescu A, Braic M, Azem FA, Titorencu I, Braic V, Pruna V, Kiss A, Parau AC, Birlik I. Effect of the deposition temperature on corrosion resistance and biocompatibility of the hydroxyapatite coatings. Appl Surf Sci 2015;354:373–9.
[90] Chen F, Lam WM, Lin CJ, Qiu GX, Wu ZH, Luk KDK, Lu WW. Biocompatibility of electrophoretical deposition of nanostructured hydroxyapatite coating on roughen titanium surface: in vitro evaluation using mesenchymal stem cells. J Biomed Mater Res B Appl Biomater 2007;82B:183–91.
[91] Heimann RB. Plasma-sprayed hydroxylapatite coatings as biocompatible intermediaries between inorganic implant surfaces and living tissue. J Therm Spray Technol 2018;27:1212–37.
[92] Büyüksağiş A, Çiftçi N. HAP coatings for biomedical applications: biocompatibility and surface protection against corrosion of Ti, Ti6Al4V and AISI 316L SS. Protect Met Phys Chem Surface 2020;56:834–43.
[93] Hernández L, González JE, Barranco V, Veranes-Pantoja Y, Galván JC, Gattorno GR. Biomimetic hydroxyapatite (HAp) coatings on pure Mg and their physiological corrosion behavior. Ceram Int 2022;48:1208–22.
[94] Yu N, Cai S, Wang F, Zhang F, Ling R, Li Y, Jiang Y, Xu G. Microwave assisted deposition of strontium doped hydroxyapatite coating on AZ31 magnesium alloy with enhanced mineralization ability and corrosion resistance. Ceram Int 2017;43:2495–503.
[95] Candidato RT, Sergi R, Jouin J, Noguera O, Pawłowski L. Advanced microstructural study of solution precursor plasma sprayed zn doped hydroxyapatite coatings. J Eur Ceram Soc 2018;38:2134–44.
[96] Lukaviciute L, Karciauskaite J, Grigoraviciute I, Vasiliauskiene D, Sokol D, Kareiva A. Calcium hydroxyapatite coatings: low-temperature synthesis and investigation of antibacterial properties. Coatings 2023;13:1991.
[97] Mróz W, Bombalska A, Burdyńska S, Jedyński M, Prokopiuk A, Budner B, Ślósarczyk A, Zima A, Menaszek E, Ścisłowska-Czarnecka A, Niedzielski K. Structural studies of magnesium doped hydroxyapatite coatings after osteoblast culture. J Mol Struct 2010;977:145–52.
[98] Liang Q, Wang W, Chen Z, Lin W. Effects of rare Earth metal oxide doping on micromorphology and corrosion behavior of hydroxyapatite-graphene oxide composite coating fabriacted on AZ91 magnesium alloy. Int J Electrochem Sci 2021;16:210647.
[99] Furko M, Havasi V, Kónya Z, Grünewald A, Detsch R, Boccaccini AR, Balázsi C. Development and characterization of multi-element doped hydroxyapatite bioceramic coatings on metallic implants for orthopedic applications. Bol Soc Espanola Ceram Vidr 2018;57:55–65.
[100] Motskin M, Wright DM, Muller K, Kyle N, Gard TG, Porter AE, Skepper JN. Hydroxyapatite nano and microparticles: correlation of particle properties with cytotoxicity and biostability. Biomaterials 2009;30:3307–17.
[101] Charkiewicz AE. Is copper still safe for us? What do we know and what are the latest literature statements? Curr Issues Mol Biol 2024;46:8441–63.
[102] Lippard SJ. Free copper ions in the cell? Science 1999;284:748–9.
[103] Li K, Xia C, Qiao Y, Liu X. Dose-response relationships between copper and its biocompatibility/antibacterial activities. J Trace Elem Med Biol 2019;55:127–35.
[104] Zhang S, Lu J, Wang Y, Verstraete W, Yuan Z, Guo J. Insights of metallic nanoparticles and ions in accelerating the bacterial uptake of antibiotic resistance genes. J Hazard Mater 2022;421:126728.